

Néel to Spin-Glass-like Phase Transition versus Dilution in Geometrically Frustrated $\text{ZnCr}_{2-2x}\text{Ga}_{2x}\text{O}_4$.

S.-H. Lee¹, W. Ratcliff II², Q. Huang², T. H. Kim³, and S-W. Cheong⁴

¹ Department of Physics, University of Virginia, Charlottesville, VA 22904

² NIST Center for Neutron Research, National Institute of Standards and Technology, Gaithersburg, Maryland 20899

³ Department of Physics and Nanosciences, EWha Womans University, Seoul 120-750, Korea and

⁴ Department of Physics and Astronomy, Rutgers University, Piscataway, New Jersey 08854

ZnCr_2O_4 undergoes a first order spin-Peierls-like phase transition at 12.5 K from a cubic spin liquid phase to a tetragonal Néel state.[1] Using powder diffraction and single crystal polarized neutron scattering, we determined the complex spin structure of the Néel phase. This phase consisted of several magnetic domains with different characteristic wave vectors. This indicates that the tetragonal phase of $\text{ZnCr}_{2-2x}\text{Ga}_{2x}\text{O}_4$ is very close to a critical point surrounded by many different Néel states. We have also studied, using elastic and inelastic neutron scattering techniques, the effect of nonmagnetic dilution on magnetic correlations in $\text{ZnCr}_{2-2x}\text{Ga}_{2x}\text{O}_4$ ($x=0.05$ and 0.3). For $x=0.05$, the magnetic correlations do not change qualitatively from those in the pure material, except that the phase transition becomes second order. For $x=0.3$, the spin-spin correlations become short range. Interestingly, the spatial correlations of the frozen spins in the $x=0.3$ material are the same as those of the fluctuating moments in the pure and the weakly diluted materials.

I. INTRODUCTION

There has been a long standing fascination in the physics community with placing antiferromagnetically coupled spins on lattices with triangular motifs.[2, 3] In two dimensions, one can consider the simple triangular lattice. When classical XY spins are placed on this lattice, it orders at zero temperature. For many years, the excitations above this ground state provided a playground for studying topological excitations. These chiral excitations destroy the ground state at finite temperatures and experimental investigations of these systems are still underway. One can increase the complexity of this problem by considering the case of the even less constrained system of corner sharing triangles, the kagome lattice.[4, 8, 9, 10, 11] There have been many theoretical questions about the nature of the ground state [12, 13, 14, 15] even for classical spins on this lattice.[5, 6, 7] Experimentally, good experimental realizations of this system have been hard to obtain. Recently, however, single crystals of Fe-jarosite that realize the kagome lattice with classical ($S = 5/2$) spins were grown and detailed neutron scattering studies have been performed.[16] More recently, $\text{ZnCu}_3(\text{OH})_6\text{Cl}_2$ was found as a good model system for the quantum kagome antiferromagnet.[17, 18, 19, 20, 21] Unfortunately, it turned out that there is 5-10% site switching of Zn^{2+} and Cu^{2+} ions,[21] which obscures the quantum physics of the kagome antiferromagnet.

In three dimensions, when spins form a network of corner sharing tetrahedra, it leads to a macroscopically degenerate ground state for classical as well as quantum spins.[22, 23] Theoretically novel low temperature properties are expected to appear. For example, quantum spin liquid phases, fractional excitations, or non-Ginzburg-Landau phase transitions. Experimentally, spinels AB_2O_4 have attracted lots of attention be-

cause the B sublattice forms a network of corner-sharing tetrahedra. In the spinel, the B site cations are octahedrally coordinated by six oxygens and neighboring BO_6 octahedra share an edge. Thus, when the B site is occupied by a transition metal ion with t_{2g} electrons, the system can realize the simple and most frustrating Heisenberg spin Hamiltonian, $H = J \sum \mathbf{S}_i \cdot \mathbf{S}_j$ with uniform nearest neighbor interactions.

ACr_2O_4 ($A = \text{Zn}[1], \text{Cd}[25], \text{Hg}[26]$) realizes the most frustrating Hamiltonian because the t_{2g} orbital of the Cr^{3+} ($3d^3$) is half filled and the nearest neighbor interactions due to the direct overlap of the neighboring t_{2g} orbitals are dominant and spatially uniform.[27] In comparison, in the case of AV_2O_4 where the V^{2+} ($3d^2$) ion has an orbital degeneracy, a Jahn-Teller distortion can occur at low temperatures, which makes the vanadates effectively one-dimensional spin chain systems.[28, 29, 30, 31] Several novel discoveries have been made in ACr_2O_4 . For instance, collective excitations of local *antiferromagnetic* hexagonal spins were found in the spin liquid phase of ZnCr_2O_4 that embody the zero-energy excitations amongst the degenerate ground states.[24, 32] Unfortunately, the lattice of ACr_2O_4 is not infinitely firm and it distorts at low temperatures to lift the magnetic frustration. The novel three-dimensional spin-Peierls phase transition, i.e., the lattice instability driven by magnetic interactions, occurs and drives the system into a Néel state. The lattice distortion can occur in different forms, depending on details of the crystal environment: tetragonal $I\bar{4}m2$ symmetry for ZnCr_2O_4 [33], tetragonal $I4_1/amd$ for CdCr_2O_4 [33], and orthorhombic $Fddd$ for HgCr_2O_4 [26, 34]. When an external magnetic field is applied to the Néel state, the half-magnetization plateau states appear in CdCr_2O_4 [35] and HgCr_2O_4 [26, 34] due to the field-induced lattice instability[36, 37].

In this paper, we investigated the nature of the 3D spin-Peierls transition in the chromite by performing elastic and inelastic neutron scattering measure-

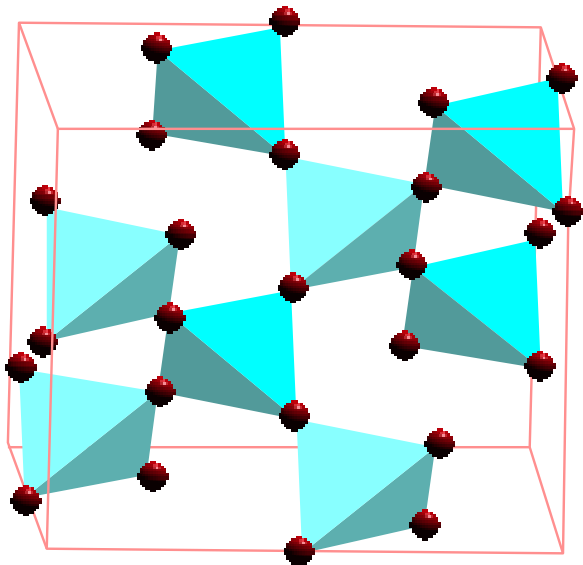


FIG. 1: Octahedral B-sites of spinel AB_2O_4 form a network of corner-sharing tetrahedra.

ments on $ZnCr_{2-2x}Ga_{2x}O_4$ for $x=0, 0.05$, and 0.3 . Our principal results are the following. For $x=0$, the Néel state has four characteristic wave vectors, $\mathbf{k} = (1, 0, 0), (\frac{1}{2}, \frac{1}{2}, \frac{1}{2}), (1, 0, \frac{1}{2})$ and $(\frac{1}{2}, \frac{1}{2}, 0)$. [38] The large size of the magnetic unit cell (64 Cr^{3+} ions) has made it difficult to uniquely determine the spin structure of this system. We have determined the spin structure, employing powder diffraction, single crystal polarized neutron diffraction data and a systematic group theoretical approach [50]. We find that the system is composed of three types of domains whose relative fractions vary from sample to sample. The dominant domain is a multi- \mathbf{k} structure with $\mathbf{k} = (1, 0, \frac{1}{2})$ and $(\frac{1}{2}, \frac{1}{2}, 0)$. This spin structure is coplanar and noncollinear with spins pointing along either the a or b axis with each tetrahedron having two pairs of antiparallel spins to have zero net moment. The $\mathbf{k} = (\frac{1}{2}, \frac{1}{2}, \frac{1}{2})$ domain has a rather simple spin structure. The spinel lattice can be decomposed into alternating kagome and triangular layers when viewed along the $\langle 111 \rangle$ direction. In this spin structure, the spins in the kagome layer order in the "q=0" configuration. The spins in the triangular layer point along the $\langle 111 \rangle$ direction and are parallel within a layer. Spins in alternating layers are antiparallel. The $\mathbf{k} = (1, 0, 0)$ domain has a collinear spin structure with spins parallel to the z -axis, as in ZnV_2O_4 . [29] In each tetrahedron the net spin is zero.

The effect of site disorder on the magnetic correlations and phase transition in $ZnCr_2O_4$ by doping nonmagnetic Ga ions into Cr sites has been previously studied by Fiorani *et al.* using bulk property measurements and neutron powder diffractions in the $ZnCr_{2-2x}Ga_{2x}O_4$ series [40]. Fig. 2 shows the phase diagram that they have constructed from the measure-

ments. Néel phase survives up to $x \sim 0.2$. For $0.2 < x < x_c$ with $1 - x_c = 0.390(3)$ being the percolation threshold for the corner-sharing tetrahedra [41], the system exhibits spin-glass-like properties in bulk susceptibility measurements. However, the nonlinear susceptibility of $ZnCr_{2-2x}Ga_{2x}O_4$ ($x=0.2$) does not display the divergence expected of an ordinary spin glass [42]. This suggests that the low temperature phase is not an ordinary spin glass.

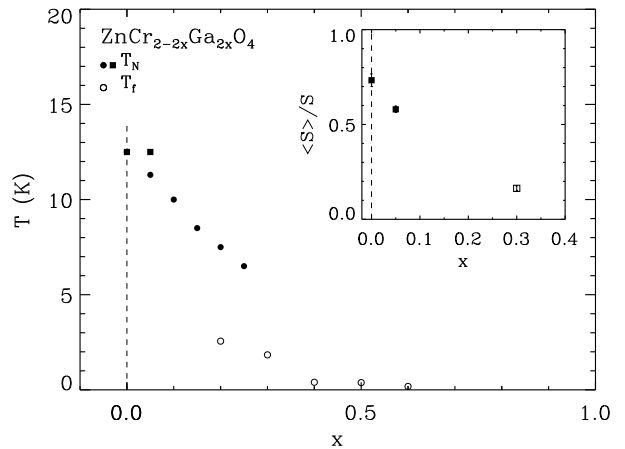


FIG. 2: Phase diagram for $ZnCr_{2-2x}Ga_{2x}O_4$. Néel temperature T_N and spin freezing temperature T_f represented by circles are the data obtained by bulk susceptibility measurements reported in Ref. [40]. T_N represented by squares and $\frac{\langle S \rangle}{S}$ in the inset are obtained by our neutron scattering measurements, which is discussed in the Sections IV and V.

Our data show that in the weakly diluted $ZnCr_{2-2x}Ga_{2x}O_4$ ($x=0.05$) Néel ordering occurs with the same spin structure as the parent compound. However, the ordering now develops gradually and the phase transition becomes second order. The appearance of the Néel ordering and the cubic-to-tetragonal structural phase now also proceed in a second order manner. This consanguinity of the order of the structural phase transition and the appearance of long-range magnetic ordering supports our interpretation that the phase transition is magnetically driven.

For $ZnCr_{2-2x}Ga_{2x}O_4$ ($x=0.3$), the magnetic long range order is replaced by static short range order even though the Cr concentration, $1 - x = 0.7$, is well above the percolation threshold, 0.390 . Interestingly, the spatial correlations of the frozen spins in the spin-glass sample are the same as those of the fluctuating moments present in the pure and weakly diluted materials. Magnetic neutron scattering intensity, $\tilde{I}(Q)$, vanishes as $Q \rightarrow 0$ and has a broad peak at $Q_c \simeq 1.5 \text{ \AA}^{-1}$ with full-width-of-half-maximum (FWHM) of $\kappa = 0.48(5) \text{ \AA}^{-1}$. This indicates that fundamental spin degree of freedom in the corner-sharing tetrahedra involves an *antiferromagnetic*

hexagonal spin loop with zero net moment, which distinguish the geometrically frustrated magnet from an ordinary spin glass.

The structure of this paper is the following: In section II, we describe the experimental details of material synthesis and the neutron scattering techniques that were used. In Section III, we explain the determination of the spin structure of $ZnCr_2O_4$. In Section IV, we discuss inelastic neutron scattering data on the material and how the spin freezing and short range spin correlations in the diluted compound resemble those in other frustrated magnets. This paper concludes with a discussion and summary in section V.

II. EXPERIMENTAL DETAILS

Three 20 g powder samples of $ZnCr_2O_4$, one $ZnCr_{1.9}Ga_{0.1}O_4$ sample and $ZnCr_{1.4}Ga_{0.6}O_4$ sample were prepared by the standard solid state reaction method with stoichiometric amounts of Cr_2O_3 , Ga_2O_3 and ZnO in air. Neutron powder diffraction measurements performed on the samples at the National Institute of Standards and Technology (NIST) BT1 diffractometer show that the samples were stoichiometric single phase spinels with the exception of one $ZnCr_2O_4$ sample (sample 2) which had a minority phase of 1% f.u. unreacted Cr_2O_3 . The results of the structural refinement are summarized in Table I. The $ZnCr_2O_4$ samples will be denoted by sample 1, sample 2, and sample 3 in this paper.

A 0.1 g single crystal of $ZnCr_2O_4$ was grown by the chemical transport method and used for polarized neutron diffraction measurements at the NIST cold neutron triple-axis spectrometer, SPINS. Spectrometer configuration was guide-PG(002)-Be-Pol.-40'-Samp.-Flip.-Pol.-40'-PG(002)-Det. The sample was mounted such that the scattering plane were the (hk0) and (h0l) zones due to twinning. A vertical guide field was applied. The polarization efficiency was determined by measuring the scattering intensities of a nuclear (2,2,0) Bragg peak with the flipper on and off. Correction for the finite polarizing efficiency, 0.85(1), was made[44].

For inelastic neutron scattering measurements on powder samples, we utilized a multiplexing detection system of SPINS consisting of a flat analyzer and a position-sensitive detector. The details of the experimental setup are reported elsewhere[1]. High angle backgrounds were measured by defocusing the analyzer while low angle backgrounds from air scattering were measured by extracting the sample from the cryostat. The absolute efficiency of the detection system was measured using incoherent elastic scattering from vanadium and nuclear Bragg peaks from the samples. The corresponding correction factor was applied to the background subtracted data to obtain normalized measurements of the magnetic scattering cross section[43].

III. ANTIFERROMAGNETIC LONG-RANGE ORDER IN $ZnCr_2O_4$

A. Powder diffraction data

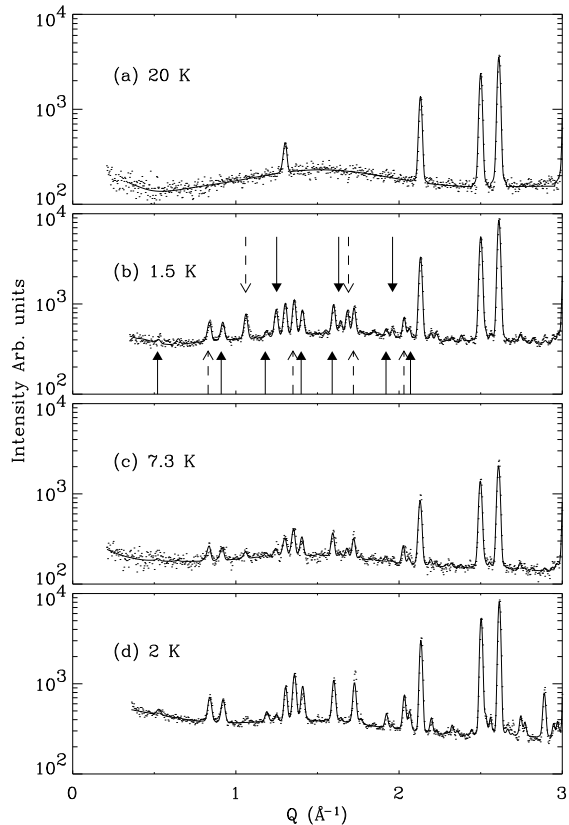


FIG. 3: Powder diffraction data from $ZnCr_2O_4$ at 25 K and 2 K taken on the powder diffractometer BT 1 at NIST. The line through the data in (a) shows the Rietveld fit to the crystal structure of which parameters are shown in Table 1. The line in (b) is the fit to the crystal structure and the magnetic structure that are explained in the text for sample 1. The upward pointing arrows with plain line are magnetic reflections which belong to $\mathbf{k} = (\frac{1}{2}, \frac{1}{2}, 0)$. From the left, they are $(\frac{1}{2}, \frac{1}{2}, 0)$, $(\frac{1}{2}, \frac{1}{2}, 1)$, $(\frac{1}{2}, \frac{3}{2}, 0)$, $(\frac{1}{2}, \frac{3}{2}, 1)$, $(\frac{1}{2}, \frac{1}{2}, 2)$ and $(\frac{3}{2}, \frac{3}{2}, 0)$, $(\frac{1}{2}, \frac{3}{2}, 2)$ and $(\frac{1}{2}, \frac{5}{2}, 0)$, and $(\frac{1}{2}, \frac{5}{2}, 1)$. The upward arrows with dashed line are magnetic reflections which belong to $\mathbf{k} = (1, 0, \frac{1}{2})$. From the left, they are $(1, 0, \frac{1}{2})$, $(1, 0, \frac{3}{2})$, $(1, 2, \frac{1}{2})$, and $(2, 1, \frac{3}{2})$ and $(1, 0, \frac{5}{2})$. The downward pointing plain arrows are from the $\mathbf{k} = (\frac{1}{2}, \frac{1}{2}, \frac{1}{2})$ family of magnetic reflections. From the left, they are $(\frac{1}{2}, \frac{1}{2}, \frac{3}{2})$, $(\frac{3}{2}, \frac{3}{2}, \frac{1}{2})$, and $(\frac{1}{2}, \frac{5}{2}, \frac{1}{2})$. The downward pointing dashed arrows are from the $\mathbf{k} = (1, 0, 0)$ family of magnetic reflections. From the left, they are $(1, 1, 0)$, $(2, 1, 0)$, and $(2, 1, 1)$. Figures (c) and (d) show the data and fits for samples (2) and (3) respectively, also discussed in the text.

Fig. 3 (a) shows $T = 25\text{K} > T_N$ diffraction data from ZnCr_2O_4 with the Rietveld fit superimposed. In addition to the nuclear Bragg reflections, there is a broad peak centered at $Q \sim 1.5 \text{ \AA}^{-1}$. This broad peak is due to dynamic spin fluctuations and will be discussed in the Section IV. Below T_c , the broad peak weakens and magnetic Bragg reflections appear, indicating a long-range magnetic ordering. These diffraction patterns are consistent with those observed previously from $\text{ZnFe}_{0.1}\text{Cr}_{1.9}\text{O}_4$ [45]. Indexing these magnetic reflections indicates that the magnetic unit cell consists of four chemical formula units (64 magnetic Cr^{3+} ions) which can be characterized by four wave vectors, $\mathbf{k} = (\frac{1}{2}, \frac{1}{2}, 0)$, $(1, 0, \frac{1}{2})$, $(\frac{1}{2}, \frac{1}{2}, \frac{1}{2})$, $(1, 0, 0)$. It is impossible to uniquely determine spin structure for a system with such a large magnetic unit cell only from its powder diffraction pattern. Olés proposed an in-plane spin structure for $\text{ZnFe}_{0.1}\text{Cr}_{1.9}\text{O}_4$ [45] and Shaked *et al.* a non-inplane structure for MgCr_2O_4 [46]. Apparently, as we will show in Section III. C, there are numerous spin structures that can explain the neutron powder diffraction data equally well. To obtain more restrictive information for the spin structure, we have performed polarized neutron diffraction on a single crystal of ZnCr_2O_4 . Our polarization study focuses on the $\mathbf{k} = (\frac{1}{2}, \frac{1}{2}, 0)$ and $(1, 0, \frac{1}{2})$ family of magnetic reflections.

B. Polarized neutron diffraction data from a single crystal

This material undergoes a cubic-to-tetragonal structural phase transition with $c < a$ at $T_N = 12.5 \text{ K}$ [1]. Because of tetragonal twinning, below T_N a wave vector transfer $\mathbf{Q} = (Q_x, Q_y, Q_z)$ in the laboratory coordinate system represents $(Q_x/a^*, Q_y/a^*, Q_z/c^*) \equiv (h, k, l)$ and $(Q_x/a^*, Q_y/c^*, Q_z/a^*) \equiv (h, l, k)$ in different crystal twin domains. In the configuration with a vertical guide field, the non-spin-flip (NSF) and spin-flip (SF) scattering cross sections, σ_{NSF} and σ_{SF} become[47, 48]

$$\begin{aligned}\sigma_{NSF} &= \sigma_N + \sigma_M^z \\ \sigma_{SF} &= \sigma_{M\perp}^x + \sigma_{M\perp}^y.\end{aligned}\quad (1)$$

Here σ_N is structural scattering cross section, and σ_M is the magnetic scattering cross section, $\sigma_M \propto (1 - \hat{\mathbf{Q}} \cdot \hat{\mathbf{S}})|F_M(\mathbf{Q})|^2$. In σ_{NSF} , we neglected the interference term between the nuclear and the magnetic scattering amplitude because the reflections considered here are either purely nuclear or purely magnetic. $F_M(\mathbf{Q})$ is the magnetic structure factor $F_M(\mathbf{Q}) = \frac{1}{2}gF(\mathbf{Q})\Sigma_d \langle S_d \rangle e^{i\mathbf{Q}\cdot\vec{d}}$ where $F(\vec{\tau})$ is the magnetic form factor of Cr^{3+} [51]. The perpendicular sign in $\sigma_{M\perp}$ is to emphasize that only the spin components perpendicular to the wave vector transfer \mathbf{Q} contribute to scattering. Fig. 3 (a) shows the NSF and SF scattering intensities obtained at a nuclear $(2,2,0)$ Bragg reflection. Only NSF scattering is expected for this nuclear Bragg reflection and the contribution in the SF channel due to the contamination

from the incomplete instrumental polarization efficiency of 0.85(1). For magnetic Bragg reflections that belong to the $\mathbf{k} = (\frac{1}{2}, \frac{1}{2}, 0)$ family, Eq. (1) becomes

$$\begin{aligned}\sigma_{NSF} &= \sigma_M^c \\ \sigma_{SF} &= \sigma_{M\perp}^a + \sigma_{M\perp}^b.\end{aligned}\quad (2)$$

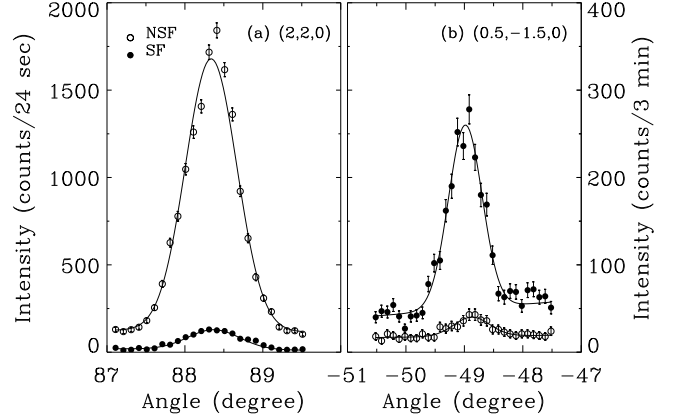


FIG. 4: Rocking scan through (a) a nuclear Bragg reflection at $(2,2,0)$ and (b) a magnetic Bragg reflection at $(\frac{1}{2}, \frac{1}{2}, 0)$ obtained from a single crystal of ZnCr_2O_4 at $T = 1.7 \text{ K}$. Open circles are the NSF data and filled ones are the SF data.

As shown in Fig. 4 (b), The magnetic $(\frac{1}{2}, \frac{1}{2}, 0)$ Bragg reflection has dominantly SF intensity and a weak signal in the NSF channel. The weak NSF intensity is due to contamination from incomplete polarization. We investigated five magnetic Bragg reflections: $(\frac{1}{2}, \frac{1}{2}, 0)$, $(\frac{1}{2}, \frac{3}{2}, 0)$, $(\frac{3}{2}, \frac{3}{2}, 0)$, $(\frac{1}{2}, \frac{5}{2}, 0)$, and $(\frac{3}{2}, \frac{5}{2}, 0)$. After the correction for the incomplete polarization, at these reflections only SF scattering is present. This means that the spins are in the ab -plane, $\sigma_M^c = 0$.

For the magnetic Bragg reflections that belong to $\mathbf{k} = (1, 0, \frac{1}{2})$, there are NSF as well as SF scattering. The ratio of SF to NSF scattering intensity, σ_{SF}/σ_{NSF} , is different at different Q , as shown in Fig. 5. Table I lists the ratios for three different reflections. The ratio, σ_{SF}/σ_{NSF} , increases as l increases. This information places a strict restriction on any possible spin configuration for ZnCr_2O_4 . For these reflections, Eq. (1) becomes

$$\begin{aligned}\sigma_{NSF} &= \sigma_M^b \\ \sigma_{SF} &= \sigma_{M\perp}^a + \sigma_{M\perp}^c.\end{aligned}\quad (3)$$

Therefore, using $\sigma_M^c = 0$,

$$\frac{\sigma_{SF}}{\sigma_{NSF}} = \left(1 - \frac{h^2}{h^2 + l^2}\right) \cdot \frac{|F_M^a|^2}{|F_M^b|^2}.\quad (4)$$

The fact that the measured σ_{SF}/σ_{NSF} follows $1 - \frac{h^2}{h^2 + l^2}$ within the experimental accuracy indicates $|F_M^a| = |F_M^b|$ for the $\mathbf{k} = (1, 0, \frac{1}{2})$ reflections.

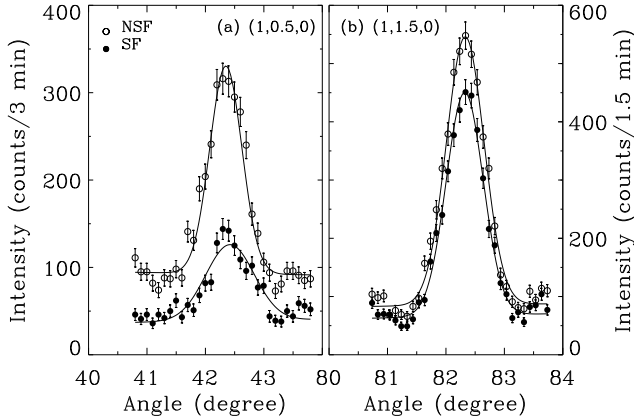


FIG. 5: Rocking scan through magnetic Bragg reflections (a) at $(1, \frac{1}{2}, 0)$ and (b) at $(1, \frac{3}{2}, 0)$ obtained from a single crystal of ZnCr_2O_4 at $T = 1.7$ K. Open circles are the NSF data and filled ones are the SF data.

C. Group theoretical approach to determination of spin structure

We have employed a group theoretical approach developed by Izyumov *et al.*[50] to determine the spin structure. The basic idea of the method is that any magnetic structure with a characteristic wave vector \mathbf{k} can be expanded in terms of basis functions, $\psi_\lambda^{\mathbf{k}L}$, of irreducible representations of the spin space of the crystal $G_{\mathbf{k}}$ which is a subgroup of the crystal space group G [50],

$$\begin{aligned} S_{0j}^{\{\mathbf{k}\}} &= \sum_L S_{0j}^{\mathbf{k}L} \\ &= \sum_L \sum_\lambda C_\lambda^{\mathbf{k}L} \psi_\lambda^{\mathbf{k}L}. \end{aligned} \quad (5)$$

Here $0j$ represents a magnetic ion at site j in zeroth primitive cell. L runs over the arms of the star \mathbf{k}_L and λ over irreducible representations of the star arm \mathbf{k}_L . The star of a wave vector \mathbf{k} , $\{\mathbf{k}\}$, is the set of nonequivalent vectors that can be obtained by acting on \mathbf{k} with an element of the crystal space group $g \in G$. For instance, the star $\{\mathbf{k}\} = \{(1, 0, \frac{1}{2})\}$ has six arms: $\mathbf{k}_L = (1, 0, \frac{1}{2}), (\bar{1}, 0, \frac{1}{2}), (1, \frac{1}{2}, 0), (\bar{1}, \frac{1}{2}, 0), (\frac{1}{2}, 0, 1)$, and $(\frac{1}{2}, 0, \bar{1})$. Once $S_{0j}^{\{\mathbf{k}\}}$ is determined, all spins at other primitive cells, S_{nj} , can be derived by[50]

$$S_{nj} = \sum_L \exp(i\mathbf{k} \cdot \mathbf{t}_n) S_{0j}^{\mathbf{k}L} \quad (6)$$

where \mathbf{t}_n is the translation vector for the n cell from the zeroth primitive cell. How to obtain the basis functions of the irreducible representations, $\psi_\lambda^{\mathbf{k}L}$ for a given $G_{\mathbf{k}}$ has been explained in a great detail in a book by Izyumov *et al.*[50] and will not be repeated here. The basis

functions $\psi_\lambda^{\mathbf{k}L}$ for $\mathbf{k} = (\frac{1}{2}, \frac{1}{2}, 0)$ and $\mathbf{k} = (1, 0, \frac{1}{2})$, are listed in Table II and III respectively. Note that $\psi_\lambda^{\mathbf{k}L}$ are complex but their simple superposition at the two arms $C_1\psi^{\mathbf{k}_1\tau} + C_2\psi^{\mathbf{k}_2\tau}$ with $\mathbf{k}_2 = -\mathbf{k}_1$ can generate a real function, provided that the coefficients C_1 and C_2 are appropriately selected. Table IV and V list such superpositions for $\mathbf{k} = (\frac{1}{2}, \frac{1}{2}, 0)$ and $\mathbf{k} = (1, 0, \frac{1}{2})$, respectively. The superpositions of two irreducible representations, $C_1\psi^{\mathbf{k}_1\tau} + C_2\psi^{\mathbf{k}_2\tau}$, do not yield nonzero spins for all 16 magnetic ions in a chemical unit cell. Instead the superposition yields four nonzero spins for $\mathbf{k} = (\frac{1}{2}, \frac{1}{2}, 0)$ and eight nonzero spins for $\mathbf{k} = (1, 0, \frac{1}{2})$ in a chemical unit cell. This means that to put all 16 nonzero spins into a chemical unit cell we have to consider at least four of the $C_1\psi^{\mathbf{k}_1\tau} + C_2\psi^{\mathbf{k}_2\tau}$ listed in Table III for $\mathbf{k} = (\frac{1}{2}, \frac{1}{2}, 0)$ and at least two of $C_1\psi^{\mathbf{k}_1\tau} + C_2\psi^{\mathbf{k}_2\tau}$ listed in Table IV for $\mathbf{k} = (1, 0, \frac{1}{2})$. Obviously the number of such combinations is very large. To narrow down the possible spin structure, we used the constraints that were obtained from polarized neutron diffraction data: (1) spins are in the ab -plane, $S_c = 0$, and (2) $|F_M^a| = |F_M^b|$ for the $(1, 0, \frac{1}{2})$ family reflections. We also assumed that (3) all spins have the same magnitude and that (4) all tetrahedra have zero net spin.

Since for this domain, there are two characteristic wave vectors involved in the Néel state of ZnCr_2O_4 , we rewrite Eq. (5) to separate $S_{0j}^{\{\mathbf{k}\}}$ into two components;

$$\begin{aligned} S_{0j}^{\{\mathbf{k}\}} &= \sum_L S_{0j}^{\mathbf{k}L(1,0,\frac{1}{2})} + \sum_L S_{0j}^{\mathbf{k}L(\frac{1}{2},\frac{1}{2},0)} \quad (7) \\ &\equiv S_{0j}^{\{\mathbf{k}(1,0,\frac{1}{2})\}} + S_{0j}^{\{\mathbf{k}(\frac{1}{2},\frac{1}{2},0)\}}. \end{aligned}$$

Note that $S^{\{\mathbf{k}(1,0,\frac{1}{2})\}}$ contribute only to the $\mathbf{k} = (1, 0, \frac{1}{2})$ family reflections and $S^{\{\mathbf{k}(\frac{1}{2},\frac{1}{2},0)\}}$ only to the $\mathbf{k} = (\frac{1}{2}, \frac{1}{2}, 0)$ reflections. Therefore we can obtain the two components separately.

First, let us consider the $\mathbf{k} = (1, 0, \frac{1}{2})$ reflections. We examined all possible combinations of the superpositions listed in Table V and found 24 different spin configurations which can be divided into three categories shown in Fig. 5. Fig. 6 (a) shows a non-collinear spin configuration in which spins are along either a -axis or b -axis, Fig. 6 (b) shows a non-collinear spin configuration with spins along $(1, \bar{1}, 0)$ or $(\bar{1}, 1, 0)$, and Fig. 6 (c) shows a collinear spin configuration along $(\bar{1}, 1, 0)$. A collinear spin configuration along a -axis or b -axis is ruled out by the constraint $|F_M^a| = |F_M^b|$.

Fig. 8 shows four prototypes of $\mathbf{k} = (\frac{1}{2}, \frac{1}{2}, 0)$ spin configurations in which all tetrahedra satisfy the antiferromagnetic constraint to have zero net moment: (100) type collinear and noncollinear spin configurations and (110) type collinear and noncollinear spin configurations.

Now, it is possible that ZnCr_2O_4 has two magnetic domains: one with $\mathbf{k} = (1, 0, \frac{1}{2})$ and the other with $\mathbf{k} = (\frac{1}{2}, \frac{1}{2}, 0)$. However, to explain the neutron powder diffraction data, the population of the two domains as well as the ordered moment have to be exactly the

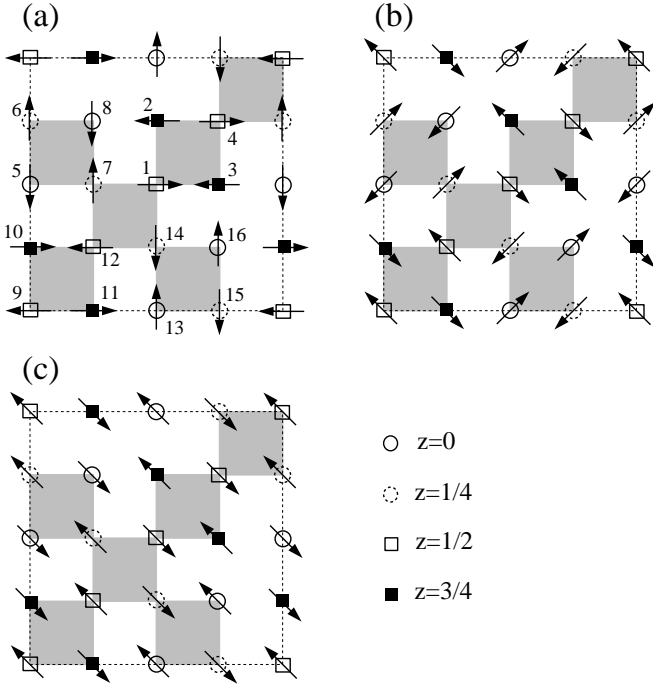


FIG. 6: Prototypes of possible spin structures in a chemical unit cell for $\mathbf{k} = (1, 0, \frac{1}{2})$ which satisfy the conditions described in the text: (a) $\psi^{\mathbf{k}_1\tau_{11}} + \psi^{\mathbf{k}_2\tau_{12}} + i\psi^{\mathbf{k}_1\tau'_{11}} - i\psi^{\mathbf{k}_2\tau'_{12}}$, (b) $(1+i)\psi^{\mathbf{k}_1\tau_{11}} + (1-i)\psi^{\mathbf{k}_2\tau_{12}} + (-1+i)\psi^{\mathbf{k}_1\tau'_{11}} + (-1-i)\psi^{\mathbf{k}_2\tau'_{12}}$, and (c) $\psi^{\mathbf{k}_1\tau_{11}} + \psi^{\mathbf{k}_2\tau_{12}} + i\psi^{\mathbf{k}_1\tau'_{11}} - i\psi^{\mathbf{k}_2\tau'_{12}} - i\psi^{\mathbf{k}_1\tau_{21}} - i\psi^{\mathbf{k}_2\tau_{22}} - \psi^{\mathbf{k}_1\tau_{21}} + \psi^{\mathbf{k}_2\tau'_{22}}$. Here $\mathbf{k}_1 = (1, 0, \frac{1}{2})$ and $\mathbf{k}_2 = (\bar{1}, 0, \frac{1}{2})$. Magnetic unit cell is doubled along the c -axis and spins change the sign in the chemical unit cell displaced by $(0,0,1)$. A shaded square represents a tetrahedron formed by four Cr^{3+} ions. Symbols represent z -coordinates of the magnetic Cr^{3+} ions.

same for both domains. Furthermore, another spinel ZnFe_2O_4 also magnetically orders at low temperatures and the Néel state has only a single characteristic wave vector $\mathbf{k} = (1, 0, \frac{1}{2})$. We believe it is more likely that the two characteristic wavevectors participate in the ordering of all the spins in ZnCr_2O_4 . Then, the resulting spin structure would be a summation of $S^{\{\mathbf{k}(1,0,\frac{1}{2})\}}$ and $S^{\{\mathbf{k}(\frac{1}{2},\frac{1}{2},0)\}}$. All Cr^{3+} ions are equivalent in this spinel crystal structure and are expected to have the same magnitude, indicating that $S^{\{\mathbf{k}(1,0,\frac{1}{2})\}}$ and $S^{\{\mathbf{k}(\frac{1}{2},\frac{1}{2},0)\}}$ have to be collinear and orthogonal to each other. Among the spin structures shown in Fig. 6 and 7, the only possibility would be the combination of $S^{\{\mathbf{k}(1,0,\frac{1}{2})\}}$ shown in Fig. 6 (c) and $S^{\{\mathbf{k}(\frac{1}{2},\frac{1}{2},0)\}}$ shown in Fig. 7 (a). Fig. 8 shows the resulting coplanar and noncollinear spin structure, in which each tetrahedra has two pairs of antiparallel spins and have zero net moment.

For the $\mathbf{k} = (\frac{1}{2}, \frac{1}{2}, \frac{1}{2})$ domain, there are many possible spin structures. From Figure 3 (b)-(d), we see that the intensities of the $\mathbf{k} = (\frac{1}{2}, \frac{1}{2}, \frac{1}{2})$ reflections relative to other propagation vectors varies from sample to sample. These reflections are strongest for sample 1 shown in Figure

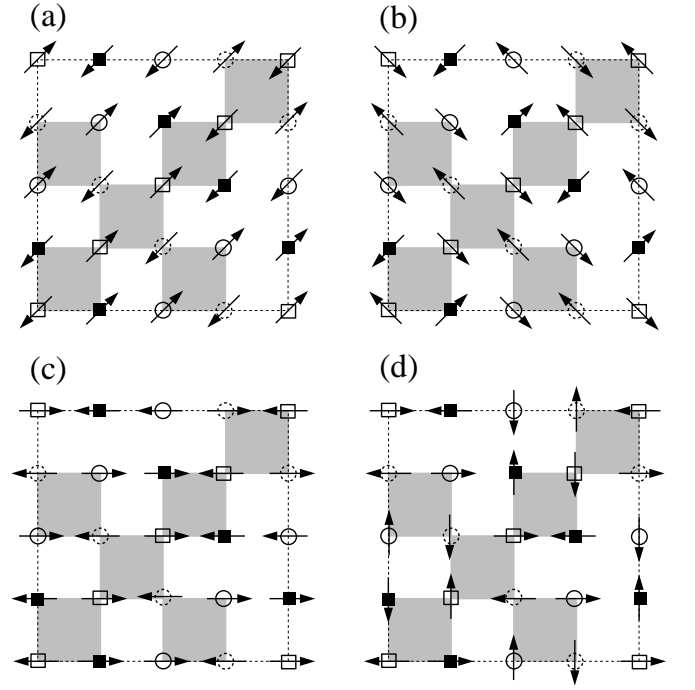


FIG. 7: Prototypes of possible spin structures in a chemical unit cell for $\mathbf{k} = (\frac{1}{2}, \frac{1}{2}, 0)$ in which satisfy the constraints described in the text: (a) $\psi^{\mathbf{k}_1\tau'_1} + i\psi^{\mathbf{k}_2\tau'_1} + (1+i)\psi^{\mathbf{k}_1\tau_2} + (1-i)\psi^{\mathbf{k}_2\tau_2} - i\psi^{\mathbf{k}_1\tau'_2} - \psi^{\mathbf{k}_2\tau'_2}$, (b) $\psi^{\mathbf{k}_1\tau'_1} + i\psi^{\mathbf{k}_2\tau'_1} + (1+i)\psi^{\mathbf{k}_1\tau_4} + (1-i)\psi^{\mathbf{k}_2\tau_4} - i\psi^{\mathbf{k}_1\tau'_4} - \psi^{\mathbf{k}_2\tau'_4}$, (c) $i\psi^{\mathbf{k}_1\tau'_1} + \psi^{\mathbf{k}_2\tau'_1} + (1-i)\psi^{\mathbf{k}_1\tau_2} + (1+i)\psi^{\mathbf{k}_2\tau_2} - \psi^{\mathbf{k}_1\tau'_2} - i\psi^{\mathbf{k}_2\tau'_2} + \psi^{\mathbf{k}_1\tau'_3} + i\psi^{\mathbf{k}_2\tau'_3} + (1+i)\psi^{\mathbf{k}_1\tau_4} + (1-i)\psi^{\mathbf{k}_2\tau_4} - i\psi^{\mathbf{k}_1\tau'_4} - \psi^{\mathbf{k}_2\tau'_4}$, and (d) $i\psi^{\mathbf{k}_1\tau'_1} + \psi^{\mathbf{k}_2\tau'_1} + (1-i)\psi^{\mathbf{k}_1\tau_2} + (1+i)\psi^{\mathbf{k}_2\tau_2} - \psi^{\mathbf{k}_1\tau'_2} - i\psi^{\mathbf{k}_2\tau'_2} - i\psi^{\mathbf{k}_1\tau'_3} - \psi^{\mathbf{k}_2\tau'_3} + (1-i)\psi^{\mathbf{k}_1\tau_4} + (1+i)\psi^{\mathbf{k}_2\tau_4} - \psi^{\mathbf{k}_1\tau'_4} - i\psi^{\mathbf{k}_2\tau'_4}$. Here $\mathbf{k}_1 = (\frac{1}{2}, \frac{1}{2}, 0)$ and $\mathbf{k}_2 = (\frac{1}{2}, \frac{1}{2}, 0)$. The magnetic unit cell is doubled along the a - and the b -axes, and spins change sign in the chemical unit cell displaced by $(1,0,0)$ or $(0,1,0)$. Symbols representing z -coordinates of the magnetic Cr^{3+} ions are the same as those in Fig. 6.

3(b) and it is only for this sample that it is possible to distinguish between various models for the spin structure through goodness of fit. Thus, our discussion will be limited to sample 1.

The basis vectors are given table VI. As the transition is first order, multiple propagation vectors can contribute to the ordering. Many can be ruled out on physical grounds, however, a large number of possibilities remain. If one visualizes the B sublattice of the spinel lattice along the $\langle 111 \rangle$ direction, one can decompose it into alternating triangular and kagome layers. The τ_1 configuration, has no spins in the triangular layer and the "q=0" spin configuration in the kagome layer. The τ_2 configuration has spins only in the triangular layer coupled antiferromagnetically. The τ_3 configuration is ferromagnetic in the kagome plane. The τ_6 configuration allows for spins in the triangular layer to lie within that

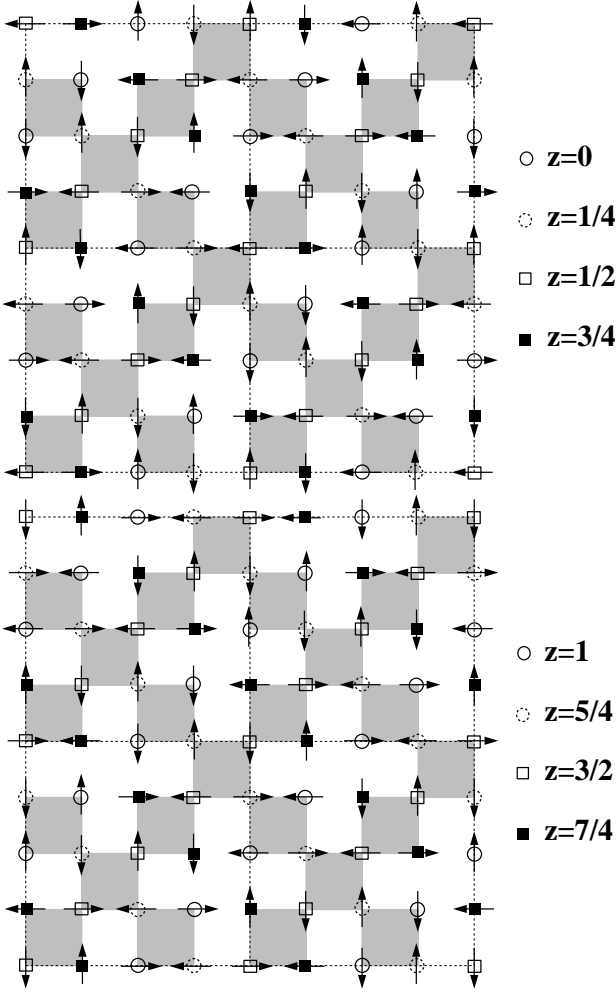


FIG. 8: A combination $S^{\{\mathbf{k}(1,0,\frac{1}{2})\}} + S^{\{\mathbf{k}(\frac{1}{2},\frac{1}{2},0)\}}$ for ZnCr_2O_4 which is consistent with all the experimental data explained in the text. Here $S^{\{\mathbf{k}(1,0,\frac{1}{2})\}} = \psi^{\mathbf{k}_1\tau_{11}} + \psi^{\mathbf{k}_2\tau_{12}} + i\psi^{\mathbf{k}_1\tau'_{11}} - i\psi^{\mathbf{k}_2\tau'_{12}} - i\psi^{\mathbf{k}_1\tau_{21}} - i\psi^{\mathbf{k}_2\tau_{22}} - \psi^{\mathbf{k}_1\tau'_{21}} + \psi^{\mathbf{k}_2\tau'_{22}}$ with $\mathbf{k}_1 = (1, 0, \frac{1}{2})$ and $\mathbf{k}_2 = (\frac{1}{2}, 0, \bar{1}, 0)$ (shown in Fig. 5 (c)), and $S^{\{\mathbf{k}(\frac{1}{2},\frac{1}{2},0)\}} = \psi^{\mathbf{k}_1\tau'_1} + i\psi^{\mathbf{k}_2\tau'_1} + (1+i)\psi^{\mathbf{k}_1\tau_2} + (1-i)\psi^{\mathbf{k}_2\tau_2} - i\psi^{\mathbf{k}_1\tau'_2} - \psi^{\mathbf{k}_2\tau'_2}$ with $\mathbf{k}_1 = (\frac{1}{2}, \frac{1}{2}, 0)$ and $\mathbf{k}_2 = (\frac{\bar{1}}{2}, \frac{\bar{1}}{2}, 0)$ (shown in Fig. 6 (a)).

plane at an arbitrary angle. We also considered linear combinations of these configurations.

In table VII, we show the relative goodness of fits for the various spin models. Overall, we found that the model most consistent with our data was one with the "q=0" configuration in the kagome layer and an antiferromagnetic configuration within the triangular layer (see Fig. 9). Though the difference in the values of χ^2 is slight, if we examine a nuclear and a magnetic peak for goodness of fit for two different configurations, $\tau_1 + \tau_2$ and $\tau_1 + \tau_2 + \tau_3$ models, we can see that there is a real improvement in the fit for the $\tau_1 + \tau_2$ spin model shown in Fig. 9 (see Fig. 10 and Table VII).

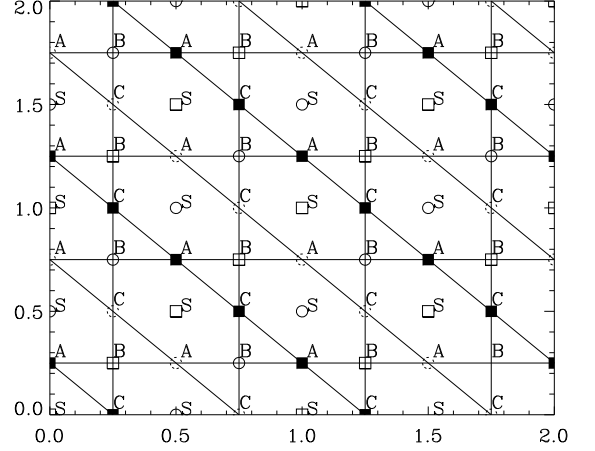


FIG. 9: This is the magnetic structure most consistent with the data for the $\mathbf{k} = (\frac{1}{2}, \frac{1}{2}, \frac{1}{2})$ propagation vector. The vertices represent spins. Spins at vertices A, B, and C lie in the kagome layer and lie within the plane and have basis vectors of $(0, 1, \bar{1})$, $(\bar{1}, 0, 1)$, and $(1, \bar{1}, 0)$ respectively. The vertices labeled by S lie in the triangular layer and the spins point along the body diagonal $(1, 1, 1)$. The spins in the triangular layer form an antiferromagnetic pattern, alternating pattern out/into of the $\langle 1, 1, 1 \rangle$ plane.

D. Summary

We have solved the magnetic structure of ZnCr_2O_4 . We have examined single crystals and three polycrystalline samples. From this, we have found that the system has different domains formed from different k-vectors. The relative phase fractions vary from sample to sample (see Table IX). The $\mathbf{k} = (1, 0, 0)$ is the same collinear structure as that of ZnV_2O_4 . The $\mathbf{k} = (1, 0, \frac{1}{2})$ and $bfk = (\frac{1}{2}, \frac{1}{2}, 0)$ domain has the in plane structure found in Fig. 8. The structure of the $\mathbf{k} = (\frac{1}{2}, \frac{1}{2}, \frac{1}{2})$ domain is found in Fig. 9. Since the antiferromagnetic transition is first order, multiple characteristic wave-vectors are allowed unlike in the usual case of second order magnetic transitions. This multiplicity of domains with different characteristic wave vectors suggests that even the ordered state of this frustrated magnet is degenerate.

IV. MAGNETIC CORRELATIONS IN $\text{ZnCr}_{2-2x}\text{Ga}_{2x}\text{O}_4$

In this section, we study how magnetic correlations change with nonmagnetic doping.

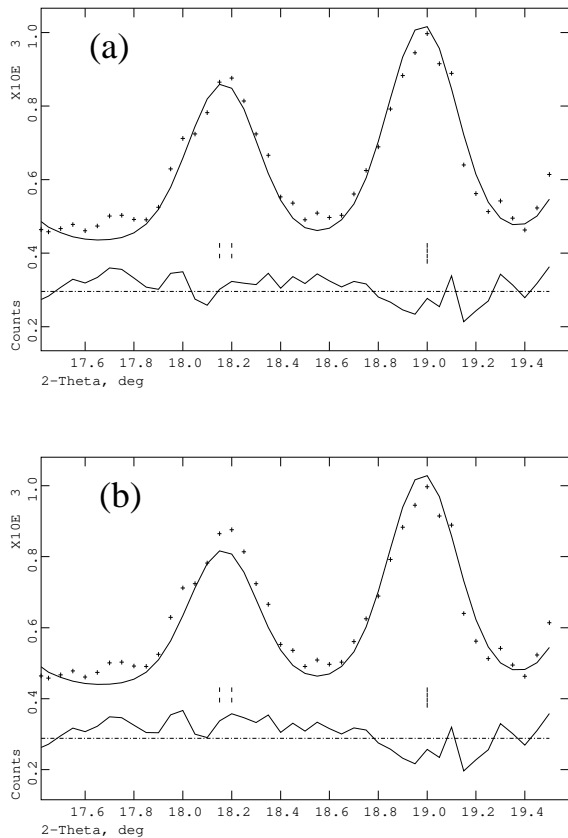


FIG. 10: The peak to the left is the $\mathbf{k} = (\frac{1}{2}, \frac{1}{2}, \frac{3}{2})$ magnetic reflection. The peak to the right is the nuclear $(1, 1, 1)$ peak for comparison. (a) the fit to the spin configuration formed from a linear combination of τ_1 and τ_2 . (b) fit to the configuration formed from a linear combination of τ_1, τ_2 , and τ_3 .

A. First order transition to Néel state in ZnCr_2O_4

For completeness, we start with the phase transition in pure ZnCr_2O_4 [1]. Fig. 10 shows that in the pure ZnCr_2O_4 long range antiferromagnetic order (squares in frame (b)) and the local spin resonance (frame (a)) appear simultaneously in a spectacular first order phase transition. It also shows that the magnetic order is accompanied by a cubic to tetragonal lattice distortion (circles in frame (b)). The tetragonal distortion lifts some of degeneracy due to geometrical frustration and allows the system to order magnetically. Furthermore the ordered state pushes spectral weight in the energy spectrum up to the local spin resonance at $\hbar\omega \approx 4.5$ meV. It is unusual that a long range ordered phase can support a local spin resonance.

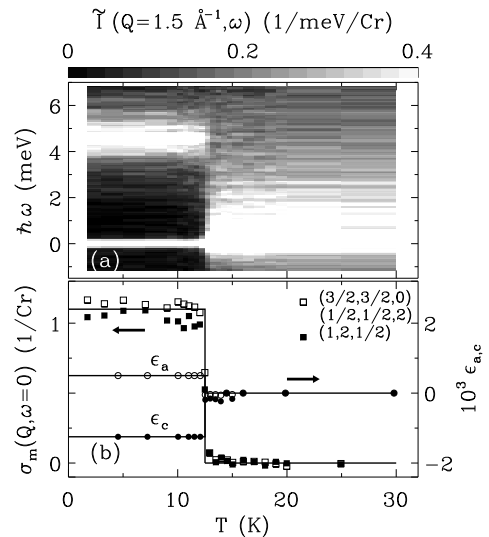


FIG. 11: Contour map of inelastic neutron scattering for $Q = 1.5 \text{ \AA}^{-1}$. (b) T -dependence of magnetic Bragg scattering from a powder (squares), $\sigma_m = \frac{v_m}{(2\pi)^3} \int \tilde{I}(Q, \omega) 4\pi Q^2 dQ d\hbar\omega$ where v_m is the volume per Cr^{3+} ion, and of lattice strain along \mathbf{a} and \mathbf{c} (circles) measured by single crystal neutron diffraction. The figure is reproduced from Ref. [1].

B. Second order transition to Néel state in $\text{ZnCr}_{1.9}\text{Ga}_{0.1}\text{O}_4$

The weak nonmagnetic doping in $\text{ZnCr}_{1.9}\text{Ga}_{0.1}\text{O}_4$ does not change the nature of the low T phase. As shown in Fig. 11, below $T_N \approx 12.5$ K magnetic long range order (squares in Fig. 11 (b)), tetragonal distortion (circles in Fig. 11 (b)) occur along with the appearance of the local spin resonance at $\hbar\omega \approx 4.5$ meV (Fig. 11 (a)). Magnetic peaks in the doped material are the same as those in ZnCr_2O_4 , which indicates that 5% doping of nonmagnetic Ga^{3+} ions into Cr sites does not change the spin structure in the ordered phase. However, the three features appear gradually in a second order fashion, which is in contrast with the first order phase transition in the pure ZnCr_2O_4 shown in Fig. 10. Fig. 11 (c) shows that as soon as the static moment develops FWHM of magnetic peaks becomes Q -resolution limited. This indicates the static correlations are long range no matter how small the static moment is. We conclude that the magnetic ordering in the weakly doped material immediately develops in the entire material rather than in small magnetic clusters, growing in size grows as T decreases.

Fig. 11 (a) shows that the local spin resonance and the low energy cooperative paramagnetic spin fluctuations coexist over the temperature range, $10 \text{ K} \leq T \leq T_N = 12.5 \text{ K}$ (also see Fig. 12 (b)). For comparison, in the pure ZnCr_2O_4 the Néel phase has only the linear spin waves below the local spin resonance (see Fig. 10 (a)). To quantitatively study how the dynamic spin fluctuations in the weakly doped system evolve with T , we have fit the of $\tilde{I}(Q=1.5 \text{ \AA}^{-1}, \hbar\omega)$ in Fig. 11 (a) to two

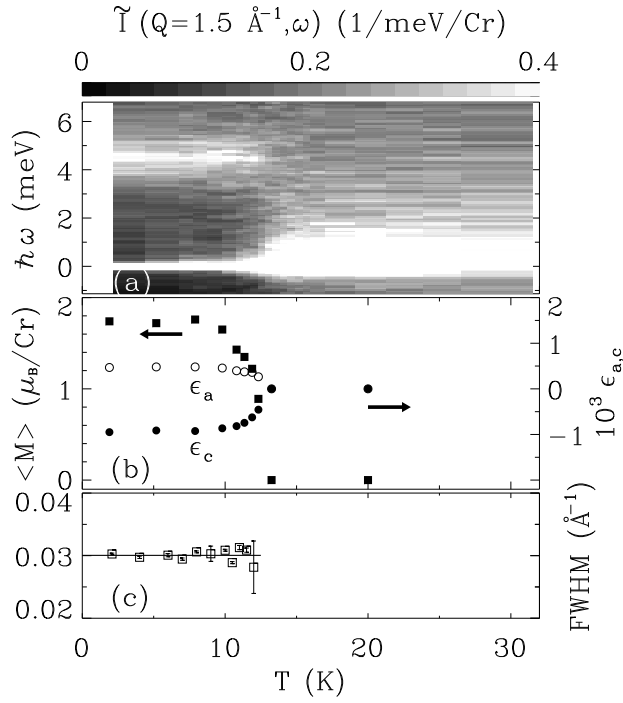


FIG. 12: Contour maps of inelastic neutron scattering measured at $Q = 1.5 \text{ \AA}^{-1}$ as a function of energy transfer $\hbar\omega$ and T . (b) T -dependence of the ordered moment (filled squares) and of crystal strains (open and filled circles) obtained by Rietveld analysis neutron powder diffraction data taken at BT1, NIST at various T s using GSAS (c) T -dependence of full-width-of-Half-Maximum (FWHM) of the magnetic $(1/2, 1/2, 2)$ Bragg peak (squares). The line is instrumental angular resolution.

simple non-resonant response functions, each with single relaxation rate: one centered at $\hbar\omega = 0$ with a relaxation rate Γ_1 and the other centered at $\hbar\omega_0 \approx 4.5 \text{ meV}$ with a relaxation rate Γ .

$$\tilde{I}(\hbar\omega) = \frac{\tilde{I}_1 \cdot (\frac{\Gamma_1}{2})^2}{(\hbar\omega)^2 + (\frac{\Gamma_1}{2})^2} + \frac{\tilde{I}_0 \cdot (\frac{\Gamma}{2})^2}{(\hbar\omega - \hbar\omega_0)^2 + (\frac{\Gamma}{2})^2}. \quad (8)$$

The first term is to account for the quasi-elastic scattering that exists at $T > 10 \text{ K}$. Since we did not have data above 30 K , it is difficult to extract meaningful information on the low energy excitations due to cooperative paramagnetism. Here we focus on the local spin resonance. Fig. 12 (d) - (f) show the results of the fits. The peak position, $\hbar\omega \approx 12.5 \text{ meV}$, (Fig. 12 (e)) is T -independent below T_N within experimental accuracy. The relaxation rate of the local resonance decreases as T decrease to $\Gamma = 1.4(1) \text{ meV}$ at 1.4 K . For comparison, in pure ZnCr_2O_4 $\Gamma = 1.5(1) \text{ meV}$ for all $T < T_N$. The strength of the local resonance, \tilde{I}_0 (Fig. 12 (d)), develops as proportional to the staggered magnetization, $\langle M \rangle$, shown is Fig. 11 (b). This suggests that the static spin component is necessary to support the local spin resonance.

Fig. 13 shows the spatial correlations of the fluctuating moments with different energies. The low energy lying

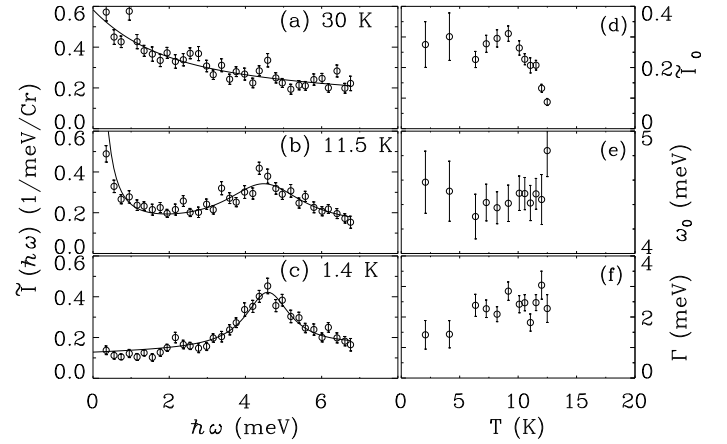


FIG. 13: (a)-(c) $\hbar\omega$ -dependence of the inelastic magnetic neutron scattering intensity measured at $Q = 1.5 \text{ \AA}^{-1}$ at three different T s spanning the phase transition. Solid lines are the fits described in the text. (d) T -dependence of integrated intensity in the unit of $(1/\text{meV}/\text{Cr})$, (e) of peak position, and (f) of full-width-at-half-maximum of the $\hbar\omega \approx 4.5 \text{ meV}$ excitations.

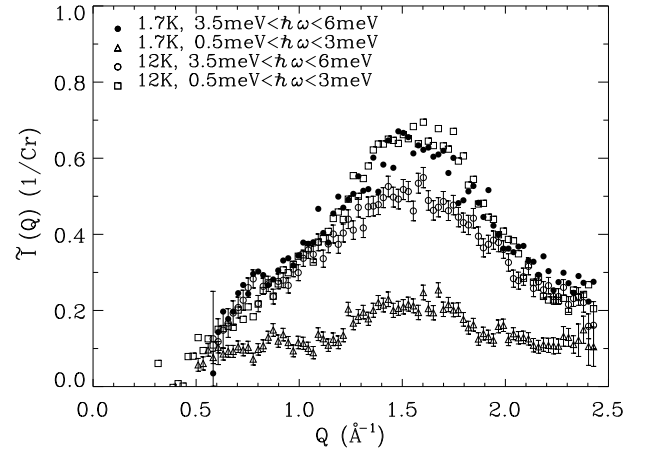


FIG. 14: Q -dependence of the inelastic magnetic neutron scattering intensity at 1.7 K and 12 K which is integrated over different energies.

excitations at 12 K (squares) and the local resonance at 1.7 K (filled circles) and 12 K (open circles) have almost identical Q -dependence with a Half Width at Half Maximum $\kappa = 0.50(5) \text{ \AA}^{-1} = 0.67(6)a^*$. Even though their characteristic energies are different, the structure factor associated with the spin fluctuations have the same wave vector dependence. The excitations for $\hbar\omega < 3 \text{ meV}$ at 1.7 K (triangles) also have a broad peak centered at $Q = 1.5 \text{ \AA}^{-1}$.

C. Spin freezing in $\text{ZnCr}_{1.4}\text{Ga}_{0.6}\text{O}_4$

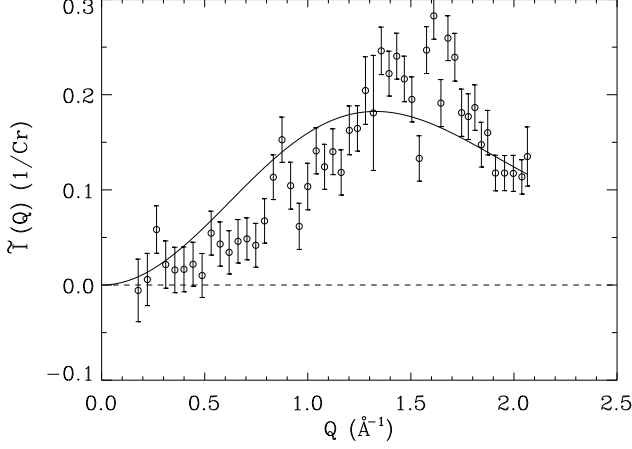


FIG. 15: Q -dependence of elastic magnetic neutron scattering intensity measured with energy window of $|\hbar\omega| < 0.05$ meV.

In this section, we study spin correlations in $\text{ZnCr}_{1.4}\text{Ga}_{0.6}\text{O}_4$ which exhibits spin-glass-like behaviors in bulk susceptibility measurements[40]. Fig. 14 shows elastic magnetic scattering intensities measured at 1.4 K. High temperature background was measured at 20 K and subtracted. Unlike in the pure ZnCr_2O_4 and the weakly doped $\text{ZnCr}_{1.9}\text{Ga}_{0.1}\text{O}_4$, this system does not have magnetic Bragg peaks but a broad peak centered at a finite wave vector $Q = 1.5 \text{ \AA}^{-1}$ with $\kappa = 0.48(5) \text{ \AA}^{-1}$. This indicates that the 30% nonmagnetic doping destroys the magnetic long range order and reduces the correlation length down to distance between nearest neighboring Cr ions. $\tilde{I}(Q)$ going to zero as Q approaches zero indicates that the antiferromagnetic constraints are still satisfied in the heavily doped sample. The solid line is the fit to the powder-averaged magnetic neutron scattering intensity for an isolated spin dimer[53, 55],

$$\tilde{I}(Q) \propto |F(Q)|^2 \frac{1 - \sin Q r_0}{Q r_0} \quad (9)$$

where the distance between nearest neighboring Cr^{3+} ions $r_0 = 2.939 \text{ \AA}$. The spin pair model produces a broader peak than the experimental data. Instead, the Q -dependence is almost identical to that of the fluctuating spins in pure ZnCr_2O_4 and weakly diluted $\text{ZnCr}_{1.9}\text{Ga}_{0.1}\text{O}_4$ (see Fig. 13). This suggests that the same local spin objects involving more than isolated dimers are responsible for the broad Q -dependence in those materials even though the energy for the correlations changes with doping of the nonmagnetic ions. We can estimate the average frozen moment from the elastic

neutron scattering data

$$|\langle M \rangle|^2 \approx \frac{\frac{3}{2}g^2 \int_{0.2\text{\AA}^{-1}}^{2.1\text{\AA}^{-1}} (\tilde{I}(Q)/|F(Q)|^2) Q^2 dQ}{\int_{0.2\text{\AA}^{-1}}^{2.1\text{\AA}^{-1}} Q^2/dQ}. \quad (10)$$

Integrating the difference data over Q yields $|\langle M \rangle|^2 = 0.24(4)\mu_B^2/\text{Cr}$, in other words, $|\langle M \rangle| = g \langle S \rangle \mu_B = 0.49(4)\mu_B/\text{Cr}$. This quantity is substantially less than the Néel value $|\langle M \rangle| = gS\mu_B = 3\mu_B/\text{Cr}$ and also much less than those values of ZnCr_2O_4 and $\text{ZnCr}_{1.9}\text{Ga}_{0.1}\text{O}_4$.

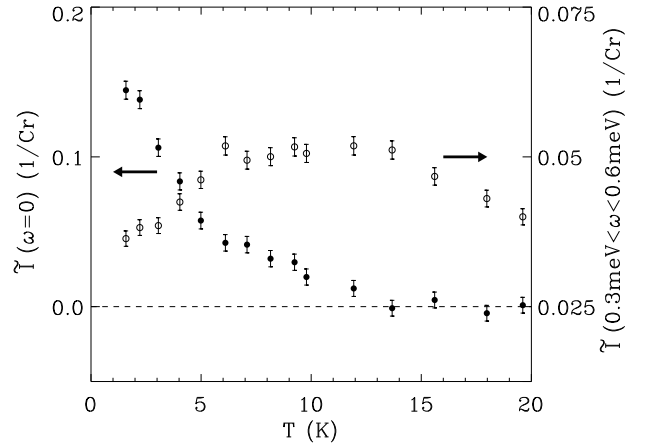


FIG. 16: T -dependence of elastic magnetic neutron scattering intensity intergerated over $|\hbar\omega| < 0.05$ meV and inelastic magnetic neutron scattering intensity integrated over $0.3 \text{ meV} < \hbar\omega < 0.6 \text{ meV}$. Both data were measured at $Q = 1.5 \text{ \AA}^{-1}$.

Fig. 15 shows elastic and inelastic neutron scattering intensities measured at $Q = 1.5 \text{ \AA}^{-1}$ as a function of temperature. The onset of elastic magnetic scattering at around 10 K signals the development of magnetic correlations on a time scale, $\tau > 2\hbar/\Delta E = 0.013 \text{ ns}$ set by the energy resolution of the instrument. Energy integrated inelastic scattering data over $0.3 \text{ meV} < \hbar\omega < 0.6 \text{ meV}$ show a broad maximum at around 10 K indicating the critical scattering at the phase transition. Bulk susceptibility data with a maximum at a lower temperature $T_f = 1.8 \text{ K}$ [40] show that this apparent critical temperature is not unique but decreases with the energy scale of the measurement. Such behavior, which is characteristic of spin glasses, indicates that a precipitous softening of the magnetic fluctuation spectrum takes place upon lowering the temperature, leading to anomalies when the lowest energy scale of the system falls below the characteristic energy scale of the measurement.

V. DISCUSSIONS AND SUMMARY

ZnCr_2O_4 is so far the best realization of an antiferromagnet on the magnetic lattice of corner-sharing tetrahedra with uniform nearest neighbor interactions and without any site-disorder. Upon cooling, this system is heading toward spin-liquid state with the signature of almost linear spin relaxation rate. At low temperature $T < T_N = 12.5$ K, the system undergoes a cubic-to-tetragonal distortion to settle into a Néel phase with a local spin resonance[1]. The three features, tetragonal distortion, long range order, and the local spin resonance, occurs abruptly in a first order fashion. The spins in the Néel phase have reduced staggered magnetization, $\frac{\langle S \rangle}{S} < 1$ (see the inset of Fig. 2) due to geometrical frustration. Weak 5% nonmagnetic doping into the magnetic lattice further suppresses the staggered magnetization but does not destroy the Néel phase at low temperatures. The phase transition from cooperative paramagnetic phase to Néel phase, however, occurs gradually upon cooling in a second order fashion. The cubic to tetragonal lattice distortion also follows the development of the magnetic phase transition. This supports that the phase transition is magnetically driven. It is understandable that the nature of the low temperature phase does not change with 5% doping because for 5% dilution in the magnetic lattice, the majority of tetrahedra have all 4 spins (81% of tetrahedra have all 4 spins and 17% have 3 spins[54]). For 30% dilution ($1-x=0.7$), 24% of tetrahedra have 4 spins, 41% have 3 spins and 27% have 2 spins. Even though it is still above the percolation threshold ($1 - x_c = 0.39$), the long range correlations are destroyed and replaced with short range correlations. Despite these differences, all three materials contain spin correlations with a common broad Q dependence even though the energetics of the local correlations change with the occupance of the magnetic lattice and the existence of long range order. This indicates that

the local spin object responsible for the common Q dependence is robust against strong disorder. This finding may explain why bulk properties in geometrically frustrated magnets are robust against dilution. In SCGO(x), where the magnetic entity relevant to geometrical frustration can be viewed as quasi-two dimensional (111)-slabs of corner-sharing tetrahedra[55], the bulk susceptibility shows field hysteresis and the nonlinear susceptibility diverges, typical of spin glasses, the specific heat $C(T)$ is proportional to T^2 as in an ordinary two-dimensional antiferromagnet[56]. These bulk behaviors are very robust against magnetic dilution.[56, 57] Our finding indicates that the fundamental spin degree of freedom in $\text{ZnCr}_{2-2x}\text{Ga}_{2x}\text{O}_4$ is the hexagonal loop of *antiferromagnetic* spins observed in the pure ZnCr_2O_4 . [24] The low energy physics is governed by the excitations of the local spin degree of freedom and therefore is robust to dilution.

In summary, we have determined the spin structure of the Néel phase in $\text{ZnCr}_{2-2x}\text{Ga}_{2x}\text{O}_4$ which would provide a starting point for a theory for this system. We have studied, using neutron scattering, how nonmagnetic doping changes the first order magnetoelastic phase transition in pure ZnCr_2O_4 into the second order spin-glass-like phase transition. We have found that a broad Q dependence is robust against dilution, suggesting that such local spin correlations both in Néel phase and in short range ordered phase is intrinsic to the geometrically frustrated magnets and distinguishes these systems from the ordinary spin glasses.

Acknowledgments

We thank C. Broholm for helpful discussions. S.H.L is supported by the U.S. DOE through DE-FG02-07ER45384. The NSF supported work at Rutgers through DMR-9802513 and work at SPINS through DMR-0454672.

-
- [1] S.-H. Lee, C. Broholm, T.H. Kim, W. Ratcliff II, and S.-W. Cheong, Phys. Rev. Lett. **84**, 3718 (2000).
 - [2] P.W. Anderson *et al*, Philos. Mag. **25**, 1 (1972).
 - [3] J. Villain, Z. Phys. B **33**, 31 (1979).
 - [4] A.P. Ramirez, "Geometrical Frustration" to appear in handbook on magnetism (2000).
 - [5] A. Chubukov, Phys. Rev. Lett. **69**, 832 (1992).
 - [6] D. A. Huse and A. D. Rutenberg Phys. Rev. B **45**, 7536 (1992).
 - [7] F. Mila, Phys. Rev. Lett. **81**, 2356 (1998).
 - [8] X. Obradors, A. Labarta, A. Isalgue, J. Tejada, J. Rodriguez, and M. Pernet, Solid State Commun. **65** 189 (1988).
 - [9] A.P. Ramirez, G.P. Espinosa, and A. S. Cooper, Phys. Rev. Lett. **64**, 2070 (1990).
 - [10] C. Broholm, G. Aeppli, G.P. Espinosa, and A.S. Cooper, Phys. Rev. Lett. **65**, 3173 (1990).
 - [11] S.-H. Lee, C. Broholm, G. Aeppli, A.P. Ramirez, T.G. Perring, C.J. Carlile, M. Adams, T.J.L. Jones, and B. Hesse, Europhys. Lett. **35**(2), 127 (1996)
 - [12] K. Park and S. Sachdev, Phys. Rev. B **65**, 220405(R) (2002).
 - [13] T. Senthil, L. Balents, S. Sachdev, A. Vishwanath, M. P. A. Fisher, Phys. Rev. B **70**, 144407 (2004).
 - [14] Y. Ran, M. Hermele, P. A. Lee, and X.-G. Wen, cond-mat/0611414.
 - [15] S. Ryu, O. I. Motrunich, J. Alicea, and M. P. A. Fisher, cond-mat/0701020.
 - [16] K. Matan, D. Grohol, D.G. Nocera, Y. Yildirim, A.B. Harris, S.-H. Lee, S.E. Nagler, Y.S. Lee, Phys. Rev. Lett. **96**, 247201 (2006).
 - [17] M. P. Shores, et al., J. Am. Chem. Soc. **127**, 13462-13463 (2005).
 - [18] J. S. Helton et al., Phys. Rev. Lett. **98**, 107204 (2007).

- [19] O. Ofer et al., Phys. Rev. Lett. **??**, ??.
- [20] P. Mendels et al., Phys. Rev. Lett. **98**, 077204 (2007).
- [21] S.-H. Lee, H. Kikuchi, Y. Qiu, B. Lake, Q. Huang, K. Habicht, and K. Kiefer, Nature Materials, in press (2007).
- [22] B. Canals and C. Lacroix, Phys. Rev. Lett. **80**, 2933 (1998); Phys. Rev. B **61**, 1149 (2000).
- [23] R. Moessner and J.T. Chalker, Phys. Rev. Lett. **80**, 2929 (1998) ; Phys. Rev. B **58**, 12049 (1998).
- [24] S.-H. Lee, C. Broholm, W. Ratcliff, G. Gasparovic, Q. Huang, T. H. Kim, and S-W. Cheong, Nature **418**, 856 (2002).
- [25] J.-H. Chung, M. Matsuda, S.-H. Lee, K. Kakurai, H. Ueda, T.J. Sato, H. Takagi, K.-P. Hong, and S. Park, Phys. Rev. Lett. **95**, 247204 (2005).
- [26] M. Matsuda, H. Ueda, A. Kikkawa, Y. Tanaka, K. Katsumata, Y. Narumi, T. Inami, Y. Ueda, S.-H. Lee, Nature Physics **3**, 397 (2007).
- [27] J.B. Goodenough, Phys. Rev. **117**, 1442 (1960).
- [28] H. Tsunetsugu and Y. Motome, Phys. Rev. B **68**, 060405(R) (2003).
- [29] S.-H. Lee, D. Louca, T. Sato, Y. Ueda, M. Isobe, S. Rosenkranz, and R. Osborn, Phys. Rev. Lett. **93**, 156407 (2004).
- [30] O. Tchernyshyov, Phys. Rev. Lett. **93**, 157206 (2004).
- [31] D. I. Khomskii and T. Mizokawa, Phys. Rev. Lett. **94**, 156402 (2005).
- [32] The formula of the hexagonal magnetic structure factor was first derived by O. Tchernyshyov *et al.* in the different context of spin waves in long range ordered phases on the spinel lattice. There it accounts for the structure factor of a nonzero-energy local antiferromagnon on *ferromagnetically* aligned hexagonal spin loops. See O. Tchernyshyov, R. Moessner, and S. L. Sondhi, Phys. Rev. Lett. **88**, 067203 (2002).
- [33] S.-H. Lee, G. Gasparovic, C. Broholm, M. Matsuda, J.-H. Chung, Y. J. Kim, H. Ueda, G. Xu, P. Zschack, K. Kakurai, H. Takagi, W. Ratcliff, T. H. Kim, and S-W. Cheong, J. of Phys. Cond. Matt. **19** (14), 145259 (2007).
- [34] H. Ueda, H. Mitamura, T. Goto, and Y. Ueda, Phys. Rev. B **73**, 094415 (2006).
- [35] H. Ueda, H. Aruga-Katori, H. Mitamura, T. Goto, and H. Takagi, Phys. Rev. Lett. **94**, 047202 (2005).
- [36] K. Penc, N. Shannon, and H. Shiba, Phys. Rev. Lett. **93**, 197203 (2004).
- [37] D. L. Bergman, R. Shindou, G. A. Fiete, and L. Balents, Phys. Rev. Lett. **96**, 097207 (2006); Phys. Rev. B **??** cond-mat/0605467 (2006).
- [38] Due to the very weak tetragonal distortion, it is not easy to determine if the half integer wavevector of $\mathbf{k} = (1, 0, \frac{1}{2})$ and the plane of the $\mathbf{k} = (1/2, 1/2, 0)$ is parallel with or perpendicular to the contracted *c*-axis. Recently, however, neutron diffraction measurements with uniaxial pressure along a few different directions proved [39] that the half integer of $\mathbf{k} = (1, 0, \frac{1}{2})$ is along the *c*-axis and the $\mathbf{k} = (1/2, 1/2, 0)$ is perpendicular to the *c*-axis.
- [39] I. Kagomiya, Y. Hata, D. Eto, H. Yanagihara, E. Kita, K. Nakajima, K. Kakurai, M. Nishi, and K. Ohoyama, J. Phys. Soc. Jpn **76**, 064710 (2007).
- [40] D. Fiorani, S. Viticoli, J. L. Dormann, J. L. Tholence, and A. P. Murani, Phys. Rev. B **30**, 2776 (1984).
- [41] F. Scholl and K. Binder, Z. Phys. B **39**, 239 (1980).
- [42] J. Hammann, D. Fiorani, M. El Yamani, and J. L. Dormann, J. Phys. C: Solid State Phys. **19**, 6635-6644 (1986).
- [43] S.-H. Lee, C. Broholm, M.F. Collins, L. Heller, A.P. Ramirez, Ch. Kloc, E. Bucher, R.W. Erwin, N. Lacey, Phys. Rev. B **56**, 8091 (1997).
- [44] C.F. Majkrzak, Physica B **221**, 342 (1996).
- [45] A. Olés, Phys. Status Solidi A **3**, 569 (1970).
- [46] H. Shaked, J. M. Hastings, and L. M. Corliss, Phys. Rev. B **1**, 3116 (1970).
- [47] R.M. Moon *et al.*, Phys. Rev. **181**, 920 (1969).
- [48] S.M. Lovesey, *Theory of Thermal Neutron Scattering from Condensed Matter*, (Clarendon Press, Oxford) 1984.
- [49] W. Schiessl, W. Potzel, H. Karzel, M. Steiner, G.M. Kalvius, A. Martin, M.K. Krause, I. Halevy, J. Gal, W. Schäfer, G. Will, M. Hillberg, and R. Wäppling, Phys. Rev. B **53**, 9143 (1996).
- [50] Yu. A. Izyumov, V. E. Naish, and R. P. Ozerov, *Neutron Diffraction of Magnetic Materials*, (Plenum Publishing Corporation, New York) 1991.
- [51] P. J. Brown, in “International Tables for Crystallography”, Volume C, edited by A. J. C. Wilson and E. Prince, Kluwer Academic Publishers Boston (1999).
- [52] O.V. Kovalev, *Representations of the Crystallographic Space Groups*, (Gordon and Breach Science Publishers) 1993.
- [53] A. Furrer and H. U. Güdel, J. Magn. Magn. Mater. **14**, 256 (1979).
- [54] R. Moessner and A. J. Berlinsky, Phys. Rev. Lett. **83**, 3293 (1999).
- [55] S.-H. Lee, C. Broholm, G. Aeppli, T.G. Perring, B. Hesse, and A. Taylor, Phys. Rev. Lett. **76**, 4424 (1996).
- [56] A.P. Ramirez, G.P. Espinosa, and A.S. Cooper, Phys. Rev. B **45**, 2505 (1992).
- [57] P. Schiffer and I. Daruka, Phys. Rev. B **56**, 13712 (1997).

TABLE I: Measured ratios of SF to NSF scattering intensities for three magnetic reflections that belong to $\mathbf{k} = (1, 0, \frac{1}{2})$.

(h, l, k)	$(\sigma_{SF}/\sigma_{NSF})_{obs}$	$1 - \frac{h^2}{h^2+l^2}$
(1,0,5,0)	0.4(1)	0.2
(1,1,5,0)	0.7(1)	0.6923
(1,2,5,0)	0.83(5)	0.862

TABLE II: The basis functions of the irreducible representation of group O_h^7 for the two-arm star of the wave vector $\mathbf{k} = (\frac{1}{2}, \frac{1}{2}, 0)$. Here \mathbf{k} is in terms of the cubic notation and $\mathbf{k} = \frac{1}{4}(2, 1, 1)$ in Kovalev's notation[52]. Here $\mathbf{k}_1 = \mathbf{k}$ and $\mathbf{k}_2 = -\mathbf{k}$. The notation of representations, such as τ_1, τ_1' and so on, followed the Kovalev's notation. $\psi_i^{\mathbf{k}\tau}$ ($i = 1, 2, 3, 4$) represent the basis functions for the spins located at $(0.5, 0.5, 0.5)$, $(0.5, 0.75, 0.75)$, $(0.75, 0.5, 0.75)$, and $(0.75, 0.75, 0.5)$ in the cubic notation, respectively. This table was taken from Table 22 in page 131 of Ref. [50].

Rep.	Arms	$\psi_1^{\mathbf{k}\tau}$	$\psi_2^{\mathbf{k}\tau}$	$\psi_3^{\mathbf{k}\tau}$	$\psi_4^{\mathbf{k}\tau}$
τ_1	k_1	$(1, \bar{1}, 0)$	$(0, 0, 0)$	$(0, 0, 0)$	$i(\bar{1}, 1, 0)$
	k_2	$(1, \bar{1}, 0)$	$(0, 0, 0)$	$(0, 0, 0)$	$-i(\bar{1}, 1, 0)$
τ_1'	k_1	$(0, 0, 0)$	$(1, 1, 0)$	$(\bar{1}, \bar{1}, 0)$	$(0, 0, 0)$
	k_2	$(0, 0, 0)$	$-i(1, 1, 0)$	$-i(\bar{1}, \bar{1}, 0)$	$(0, 0, 0)$
τ_2	k_1	$(1, 1, 0)$	$(0, 0, 0)$	$(0, 0, 0)$	$i(1, 1, 0)$
	k_2	$(1, 1, 0)$	$(0, 0, 0)$	$(0, 0, 0)$	$-i(1, 1, 0)$
τ_2'	k_1	$(0, 0, 0)$	$(1, 1, 0)$	$(1, 1, 0)$	$(0, 0, 0)$
	k_2	$(0, 0, 0)$	$-i(1, 1, 0)$	$-i(1, 1, 0)$	$(0, 0, 0)$
τ_2''	k_1	$(0, 0, 1)$	$(0, 0, 0)$	$(0, 0, 0)$	$i(0, 0, \bar{1})$
	k_2	$(0, 0, 1)$	$(0, 0, 0)$	$(0, 0, 0)$	$-i(0, 0, \bar{1})$
τ_3	k_1	$(1, 1, 0)$	$(0, 0, 0)$	$(0, 0, 0)$	$i(\bar{1}, \bar{1}, 0)$
	k_2	$(1, 1, 0)$	$(0, 0, 0)$	$(0, 0, 0)$	$-i(\bar{1}, \bar{1}, 0)$
τ_3'	k_1	$(0, 0, 0)$	$(1, \bar{1}, 0)$	$(\bar{1}, 1, 0)$	$(0, 0, 0)$
	k_2	$(0, 0, 0)$	$-i(1, \bar{1}, 0)$	$-i(\bar{1}, 1, 0)$	$(0, 0, 0)$
τ_3''	k_1	$(0, 0, 1)$	$(0, 0, 0)$	$(0, 0, 0)$	$i(0, 0, 1)$
	k_2	$(0, 0, 1)$	$(0, 0, 0)$	$(0, 0, 0)$	$-i(0, 0, 1)$
τ_3'''	k_1	$(0, 0, 0)$	$(0, 0, 1)$	$(0, 0, 1)$	$(0, 0, 0)$
	k_2	$(0, 0, 0)$	$-i(0, 0, 1)$	$-i(0, 0, 1)$	$(0, 0, 0)$
τ_4	k_1	$(1, \bar{1}, 0)$	$(0, 0, 0)$	$(0, 0, 0)$	$i(1, \bar{1}, 0)$
	k_2	$(1, \bar{1}, 0)$	$(0, 0, 0)$	$(0, 0, 0)$	$-i(1, \bar{1}, 0)$
τ_4'	k_1	$(0, 0, 0)$	$(1, \bar{1}, 0)$	$(1, \bar{1}, 0)$	$(0, 0, 0)$
	k_2	$(0, 0, 0)$	$-i(1, \bar{1}, 0)$	$-i(1, \bar{1}, 0)$	$(0, 0, 0)$
τ_4''	k_1	$(0, 0, 0)$	$(0, 0, 1)$	$(0, 0, \bar{1})$	$(0, 0, 0)$
	k_2	$(0, 0, 0)$	$-i(0, 0, 1)$	$-i(0, 0, \bar{1})$	$(0, 0, 0)$

TABLE III: The basis functions of the irreducible representation of group $Fd\bar{3}m(O_h^7)$ for the two-arm star of the wave vector $\mathbf{k} = (1, 0, \frac{1}{2})$. Here \mathbf{k} is in terms of the cubic notation and $\mathbf{k} = \frac{1}{4}(1, 1, 0) + \frac{1}{2}(0, 1, 1)$ in Kovalev's notation using primitive reciprocal unit vectors [52]. Here $\mathbf{k}_1 = \mathbf{k}$ and $\mathbf{k}_2 = -\mathbf{k}$. The notation of representations, such as τ_1, τ_1' and so on, followed the Kovalev's notation. $\psi_i^{\mathbf{k}\tau}$ ($i = 1, 2, 3, 4$) represent the basis functions for four spins in the primitive cell located at $(0.5, 0.5, 0.5)$, $(0.5, 0.75, 0.75)$, $(0.75, 0.5, 0.75)$, and $(0.75, 0.75, 0.5)$ in the cubic notation, respectively.

Rep.	Arms	$\psi_1^{\mathbf{k}\tau}$	$\psi_2^{\mathbf{k}\tau}$	$\psi_3^{\mathbf{k}\tau}$	$\psi_4^{\mathbf{k}\tau}$
τ_{11}	k_1	(1, 0, 0)	$-i(0, 1, 0)$	$-i(0, 1, 0)$	(1, 0, 0)
	k_2	($\bar{1}$, 0, 0)	(0, 1, 0)	(0, $\bar{1}$, 0)	(1, 0, 0)
τ_{12}	k_1	($\bar{1}$, 0, 0)	(0, 1, 0)	(0, $\bar{1}$, 0)	(1, 0, 0)
	k_2	(1, 0, 0)	$i(0, 1, 0)$	$i(0, 1, 0)$	(1, 0, 0)
τ_{11}'	k_1	(0, 1, 0)	$i(1, 0, 0)$	$i(1, 0, 0)$	(0, 1, 0)
	k_2	(0, $\bar{1}$, 0)	($\bar{1}$, 0, 0)	(1, 0, 0)	(0, 1, 0)
τ_{12}'	k_1	(0, $\bar{1}$, 0)	($\bar{1}$, 0, 0)	(1, 0, 0)	(0, 1, 0)
	k_2	(0, 1, 0)	$-i(1, 0, 0)$	$-i(1, 0, 0)$	(0, 1, 0)
τ_{11}''	k_1	(0, 0, 1)	$-i(0, 0, 1)$	$i(0, 0, 1)$	(0, 0, $\bar{1}$)
	k_2	(0, 0, $\bar{1}$)	(0, 0, 1)	(0, 0, 1)	(0, 0, $\bar{1}$)
τ_{12}''	k_1	(0, 0, $\bar{1}$)	(0, 0, 1)	(0, 0, 1)	(0, 0, $\bar{1}$)
	k_2	(0, 0, 1)	$i(0, 0, 1)$	$-i(0, 0, 1)$	(0, 0, $\bar{1}$)
τ_{21}	k_1	(1, 0, 0)	$i(0, 1, 0)$	$i(0, 1, 0)$	(1, 0, 0)
	k_2	($\bar{1}$, 0, 0)	(0, $\bar{1}$, 0)	(0, 1, 0)	(1, 0, 0)
τ_{22}	k_1	(1, 0, 0)	(0, 1, 0)	(0, $\bar{1}$, 0)	($\bar{1}$, 0, 0)
	k_2	($\bar{1}$, 0, 0)	$i(0, 1, 0)$	$i(0, 1, 0)$	($\bar{1}$, 0, 0)
τ_{21}'	k_1	(0, 1, 0)	$i(\bar{1}, 0, 0)$	$i(\bar{1}, 0, 0)$	(0, 1, 0)
	k_2	(0, $\bar{1}$, 0)	(1, 0, 0)	($\bar{1}$, 0, 0)	(0, 1, 0)
τ_{22}'	k_1	(0, 1, 0)	($\bar{1}$, 0, 0)	(1, 0, 0)	(0, $\bar{1}$, 0)
	k_2	(0, $\bar{1}$, 0)	$-i(1, 0, 0)$	$-i(1, 0, 0)$	(0, $\bar{1}$, 0)
τ_{21}''	k_1	(0, 0, 1)	$i(0, 0, 1)$	$-i(0, 0, 1)$	(0, 0, $\bar{1}$)
	k_2	(0, 0, $\bar{1}$)	(0, 0, $\bar{1}$)	(0, 0, $\bar{1}$)	(0, 0, $\bar{1}$)
τ_{22}''	k_1	(0, 0, 1)	(0, 0, 1)	(0, 0, 1)	(0, 0, 1)
	k_2	(0, 0, $\bar{1}$)	$i(0, 0, 1)$	$-i(0, 0, 1)$	(0, 0, 1)

TABLE IV: Superpositions of two irreducible representations, $C_1\psi^{\mathbf{k}_1\tau} + C_2\psi^{\mathbf{k}_2\tau}$, which give real spins to the atoms for $\mathbf{k}_1 = (\frac{1}{2}, \frac{1}{2}, 0)$ and $\mathbf{k}_2 = -\mathbf{k}_1$. $1(1, \bar{1}, 0)$ represents the spin at site 1 is along $(1, \bar{1}, 0)$. Positions of the 1 to 16 sites are shown in Fig. 6 (a).

Superposition	Nonzero spins in a chemical unit cell			
$k_1\tau_1 + k_2\tau_1$	$1(1, \bar{1}, 0)$	$8(\bar{1}, 1, 0)$	$9(\bar{1}, 1, 0)$	$16(\bar{1}, 1, 0)$
$-ik_1\tau_1 + ik_2\tau_1$	$4(\bar{1}, 1, 0)$	$5(\bar{1}, 1, 0)$	$12(1, \bar{1}, 0)$	$13(\bar{1}, 1, 0)$
$k_1\tau_1' + ik_2\tau_1'$	$2(1, 1, 0)$	$3(\bar{1}, \bar{1}, 0)$	$10(\bar{1}, \bar{1}, 0)$	$11(1, 1, 0)$
$ik_1\tau_1' + k_2\tau_1'$	$6(1, 1, 0)$	$7(\bar{1}, \bar{1}, 0)$	$14(1, 1, 0)$	$15(\bar{1}, \bar{1}, 0)$
$k_1\tau_2 + k_2\tau_2$	$1(1, 1, 0)$	$8(1, 1, 0)$	$9(\bar{1}, \bar{1}, 0)$	$16(1, 1, 0)$
$-ik_1\tau_2 + ik_2\tau_2$	$4(1, 1, 0)$	$5(\bar{1}, \bar{1}, 0)$	$12(\bar{1}, \bar{1}, 0)$	$13(\bar{1}, \bar{1}, 0)$
$k_1\tau_2' + ik_2\tau_2'$	$2(1, 1, 0)$	$3(1, 1, 0)$	$10(\bar{1}, \bar{1}, 0)$	$11(\bar{1}, \bar{1}, 0)$
$ik_1\tau_2' + k_2\tau_2'$	$6(1, 1, 0)$	$7(1, 1, 0)$	$14(1, 1, 0)$	$15(1, 1, 0)$
$k_1\tau_2'' + k_2\tau_2''$	$1(0, 0, 1)$	$8(0, 0, \bar{1})$	$9(0, 0, \bar{1})$	$16(0, 0, \bar{1})$
$-ik_1\tau_2'' + ik_2\tau_2''$	$4(0, 0, \bar{1})$	$5(0, 0, \bar{1})$	$12(0, 0, 1)$	$13(0, 0, \bar{1})$
$k_1\tau_3 + k_2\tau_3$	$1(1, 1, 0)$	$8(\bar{1}, \bar{1}, 0)$	$9(\bar{1}, \bar{1}, 0)$	$16(\bar{1}, \bar{1}, 0)$
$-ik_1\tau_3 + ik_2\tau_3$	$4(\bar{1}, \bar{1}, 0)$	$5(\bar{1}, \bar{1}, 0)$	$12(1, 1, 0)$	$13(\bar{1}, \bar{1}, 0)$
$k_1\tau_3' + ik_2\tau_3'$	$2(1, \bar{1}, 0)$	$3(\bar{1}, 1, 0)$	$10(\bar{1}, 1, 0)$	$11(1, \bar{1}, 0)$
$ik_1\tau_3' + k_2\tau_3'$	$6(1, \bar{1}, 0)$	$7(\bar{1}, 1, 0)$	$14(1, \bar{1}, 0)$	$15(\bar{1}, 1, 0)$
$k_1\tau_3'' + k_2\tau_3''$	$1(0, 0, 1)$	$8(0, 0, 1)$	$9(0, 0, \bar{1})$	$16(0, 0, 1)$
$-ik_1\tau_3'' + ik_2\tau_3''$	$4(0, 0, 1)$	$5(0, 0, \bar{1})$	$12(0, 0, \bar{1})$	$13(0, 0, \bar{1})$
$k_1\tau_3''' + ik_2\tau_3'''$	$2(0, 0, 1)$	$3(0, 0, 1)$	$10(0, 0, \bar{1})$	$11(0, 0, \bar{1})$
$ik_1\tau_3''' + k_2\tau_3'''$	$6(0, 0, 1)$	$7(0, 0, 1)$	$14(0, 0, 1)$	$15(0, 0, 1)$
$k_1\tau_4 + k_2\tau_4$	$1(1, \bar{1}, 0)$	$8(1, \bar{1}, 0)$	$9(\bar{1}, 1, 0)$	$16(1, \bar{1}, 0)$
$-ik_1\tau_4 + ik_2\tau_4$	$4(1, \bar{1}, 0)$	$5(\bar{1}, 1, 0)$	$12(\bar{1}, 1, 0)$	$13(\bar{1}, 1, 0)$
$k_1\tau_4' + ik_2\tau_4'$	$2(1, \bar{1}, 0)$	$3(1, \bar{1}, 0)$	$10(\bar{1}, 1, 0)$	$11(\bar{1}, 1, 0)$
$ik_1\tau_4' + k_2\tau_4'$	$6(1, \bar{1}, 0)$	$7(1, \bar{1}, 0)$	$14(1, \bar{1}, 0)$	$15(1, \bar{1}, 0)$
$k_1\tau_4'' + ik_2\tau_4''$	$2(0, 0, 1)$	$3(0, 0, \bar{1})$	$10(0, 0, \bar{1})$	$11(0, 0, 1)$
$ik_1\tau_4'' + k_2\tau_4''$	$6(0, 0, 1)$	$7(0, 0, \bar{1})$	$14(0, 0, 1)$	$15(0, 0, \bar{1})$

TABLE V: Superpositions of two irreducible representations, $C_1\psi^{\mathbf{k}_1\tau} + C_2\psi^{\mathbf{k}_2\tau}$, which give real spins to the atoms for $\mathbf{k}_1 = (1, 0, \frac{1}{2})$ and $\mathbf{k}_2 = -\mathbf{k}_1$.

Superposition	Nonzero spins in a chemical unit cell							
$k_1\tau_{11} + k_2\tau_{12}$	1(1, 0, 0)	4(1, 0, 0)	6(0, 1, 0)	7(0, 1, 0)	9($\bar{1}$, 0, 0)	12($\bar{1}$, 0, 0)	14(0, $\bar{1}$, 0)	15(0, $\bar{1}$, 0)
$-ik_1\tau_{11} + ik_2\tau_{12}$	2(0, $\bar{1}$, 0)	3(0, $\bar{1}$, 0)	5(1, 0, 0)	8(1, 0, 0)	10(0, 1, 0)	11(0, 1, 0)	13($\bar{1}$, 0, 0)	16($\bar{1}$, 0, 0)
$k_1\tau_{12} + k_2\tau_{11}$	1($\bar{1}$, 0, 0)	2(0, 1, 0)	3(0, $\bar{1}$, 0)	4(1, 0, 0)	9(1, 0, 0)	10(0, $\bar{1}$, 0)	11(0, 1, 0)	12($\bar{1}$, 0, 0)
$-ik_1\tau_{12} + ik_2\tau_{11}$	5($\bar{1}$, 0, 0)	6(0, 1, 0)	7(0, $\bar{1}$, 0)	8(1, 0, 0)	13(1, 0, 0)	14(0, $\bar{1}$, 0)	15(0, 1, 0)	16($\bar{1}$, 0, 0)
$k_1\tau'_{11} + k_2\tau'_{12}$	1(0, 1, 0)	4(0, 1, 0)	6($\bar{1}$, 0, 0)	7($\bar{1}$, 0, 0)	9(0, $\bar{1}$, 0)	12(0, $\bar{1}$, 0)	14(1, 0, 0)	15(1, 0, 0)
$-ik_1\tau'_{11} + ik_2\tau'_{12}$	2(1, 0, 0)	3(1, 0, 0)	5(0, 1, 0)	8(0, 1, 0)	10($\bar{1}$, 0, 0)	11($\bar{1}$, 0, 0)	13(0, $\bar{1}$, 0)	16(0, $\bar{1}$, 0)
$k_1\tau'_{12} + k_2\tau'_{11}$	1(0, $\bar{1}$, 0)	2($\bar{1}$, 0, 0)	3(1, 0, 0)	4(0, 1, 0)	9(0, 1, 0)	10(1, 0, 0)	11($\bar{1}$, 0, 0)	12(0, $\bar{1}$, 0)
$-ik_1\tau'_{12} + ik_2\tau'_{11}$	5(0, $\bar{1}$, 0)	6($\bar{1}$, 0, 0)	7(1, 0, 0)	8(0, 1, 0)	13(0, 1, 0)	14(1, 0, 0)	15($\bar{1}$, 0, 0)	16(0, $\bar{1}$, 0)
$k_1\tau''_{11} + k_2\tau''_{12}$	1(0, 0, 1)	4(0, 0, $\bar{1}$)	6(0, 0, 1)	7(0, 0, $\bar{1}$)	9(0, 0, $\bar{1}$)	12(0, 0, 1)	14(0, 0, $\bar{1}$)	15(0, 0, 1)
$-ik_1\tau''_{11} + ik_2\tau''_{12}$	2(0, 0, $\bar{1}$)	3(0, 0, 1)	5(0, 0, 1)	8(0, 0, $\bar{1}$)	10(0, 0, 1)	11(0, 0, $\bar{1}$)	13(0, 0, $\bar{1}$)	16(0, 0, 1)
$k_1\tau''_{12} + k_2\tau''_{11}$	1(0, 0, $\bar{1}$)	2(0, 0, 1)	3(0, 0, 1)	4(0, 0, $\bar{1}$)	9(0, 0, 1)	10(0, 0, $\bar{1}$)	11(0, 0, $\bar{1}$)	12(0, 0, 1)
$-ik_1\tau''_{12} + ik_2\tau''_{11}$	5(0, 0, $\bar{1}$)	6(0, 0, 1)	7(0, 0, 1)	8(0, 0, $\bar{1}$)	13(0, 0, 1)	14(0, 0, $\bar{1}$)	15(0, 0, $\bar{1}$)	16(0, 0, 1)
$k_1\tau_{21} - k_2\tau_{22}$	1(1, 0, 0)	4(1, 0, 0)	6(0, $\bar{1}$, 0)	7(0, $\bar{1}$, 0)	9($\bar{1}$, 0, 0)	12($\bar{1}$, 0, 0)	14(0, 1, 0)	15(0, 1, 0)
$ik_1\tau_{21} + ik_2\tau_{22}$	2(0, $\bar{1}$, 0)	3(0, $\bar{1}$, 0)	5($\bar{1}$, 0, 0)	8($\bar{1}$, 0, 0)	10(0, 1, 0)	11(0, 1, 0)	13(1, 0, 0)	16(1, 0, 0)
$-k_1\tau_{22} + k_2\tau_{21}$	1($\bar{1}$, 0, 0)	2(0, $\bar{1}$, 0)	3(0, 1, 0)	4(1, 0, 0)	9(1, 0, 0)	10(0, 1, 0)	11(0, $\bar{1}$, 0)	12($\bar{1}$, 0, 0)
$ik_1\tau_{22} + ik_2\tau_{21}$	5($\bar{1}$, 0, 0)	6(0, $\bar{1}$, 0)	7(0, 1, 0)	8(1, 0, 0)	13(1, 0, 0)	14(0, 1, 0)	15(0, $\bar{1}$, 0)	16($\bar{1}$, 0, 0)
$k_1\tau_{21} - k_2\tau_{22}$	1(0, 1, 0)	4(0, 1, 0)	6(1, 0, 0)	7(1, 0, 0)	9(0, $\bar{1}$, 0)	12(0, $\bar{1}$, 0)	14($\bar{1}$, 0, 0)	15($\bar{1}$, 0, 0)
$ik_1\tau_{21} + ik_2\tau_{22}$	2(1, 0, 0)	3(1, 0, 0)	5(0, $\bar{1}$, 0)	8(0, $\bar{1}$, 0)	10($\bar{1}$, 0, 0)	11($\bar{1}$, 0, 0)	13(0, 1, 0)	16(0, 1, 0)
$k_1\tau'_{22} - k_2\tau'_{21}$	1(0, 1, 0)	2($\bar{1}$, 0, 0)	3(1, 0, 0)	4(0, $\bar{1}$, 0)	9(0, $\bar{1}$, 0)	10(1, 0, 0)	11($\bar{1}$, 0, 0)	12(0, 1, 0)
$ik_1\tau'_{22} + ik_2\tau'_{21}$	5(0, $\bar{1}$, 0)	6(1, 0, 0)	7($\bar{1}$, 0, 0)	8(0, 1, 0)	13(0, 1, 0)	14($\bar{1}$, 0, 0)	15(1, 0, 0)	16(0, $\bar{1}$, 0)
$k_1\tau''_{21} - k_2\tau''_{22}$	1(0, 0, 1)	4(0, 0, $\bar{1}$)	6(0, 0, $\bar{1}$)	7(0, 0, 1)	9(0, 0, $\bar{1}$)	12(0, 0, 1)	14(0, 0, 1)	15(0, 0, $\bar{1}$)
$ik_1\tau''_{21} + ik_2\tau''_{22}$	2(0, 0, $\bar{1}$)	3(0, 0, 1)	5(0, 0, $\bar{1}$)	8(0, 0, 1)	10(0, 0, 1)	11(0, 0, $\bar{1}$)	13(0, 0, 1)	16(0, 0, $\bar{1}$)
$k_1\tau''_{22} - k_2\tau''_{21}$	1(0, 0, 1)	2(0, 0, 1)	3(0, 0, 1)	4(0, 0, 1)	9(0, 0, $\bar{1}$)	10(0, 0, $\bar{1}$)	11(0, 0, $\bar{1}$)	12(0, 0, $\bar{1}$)
$ik_1\tau''_{22} + ik_2\tau''_{21}$	5(0, 0, $\bar{1}$)	6(0, 0, $\bar{1}$)	7(0, 0, $\bar{1}$)	8(0, 0, 1)	13(0, 0, 1)	14(0, 0, 1)	15(0, 0, 1)	16(0, 0, 1)

TABLE VI: The basis functions of the irreducible representation of group $Fd\bar{3}m(O_h^7)$ for the two-arm star of the wave vector $\mathbf{k} = (\frac{1}{2}, \frac{1}{2}, \frac{1}{2})$.

Rep.	$\psi_1^{\mathbf{k}\tau}$	$\psi_2^{\mathbf{k}\tau}$	$\psi_3^{\mathbf{k}\tau}$	$\psi_4^{\mathbf{k}\tau}$
τ_1	(0, 0, 0)	(0, 1, $\bar{1}$)	($\bar{1}$, 0, 1)	(1, $\bar{1}$, 0)
τ_2	(1, 1, 1)	(0, 0, 0)	(0, 0, 0)	(0, 0, 0)
τ_3	(0, 0, 0)	(1, 0, 0)	(0, 1, 0)	(0, 0, 1)
	(0, 0, 0)	(0, 1, 1)	(1, 0, 1)	(1, 1, 0)
τ_5	(0, 0, 0)	(2, 0, 0)	(0, $\bar{1}$, 0)	(0, 0, $\bar{1}$)
	(0, 0, 0)	(0, 2, 0)	(0, 0, $\bar{1}$)	($\bar{1}$, 0, 0)
	(0, 0, 0)	(0, 0, 2)	($\bar{1}$, 0, 0)	(0, $\bar{1}$, 0)
	(0, 0, 0)	($\bar{1}$, 0, 0)	(0, 2, 0)	(0, 0, $\bar{1}$)
	(0, 0, 0)	(0, 0, $\bar{1}$)	(2, 0, 0)	(0, $\bar{1}$, 0)
	(0, 0, 0)	(0, $\bar{1}$, 0)	(0, 0, 2)	($\bar{1}$, 0, 0)
	(0, 0, 0)	(1, 0, 0)	(0, 1, 0)	(0, 0, $\bar{2}$)
	(0, 0, 0)	(0, 1, 0)	(0, 0, 1)	($\bar{2}$, 0, 0)
	(0, 0, 0)	(0, 0, 1)	(1, 0, 0)	(0, $\bar{2}$, 0)
τ_6	(2, $\bar{1}$, $\bar{1}$)	(0, 0, 0)	(0, 0, 0)	(0, 0, 0)
	(0, 1, $\bar{1}$)	(0, 0, 0)	(0, 0, 0)	(0, 0, 0)

TABLE VII: Goodness of the fit of the different spin models with $\mathbf{k} = (\frac{1}{2}, \frac{1}{2}, \frac{1}{2})$ to the $\{\frac{1}{2}, \frac{1}{2}, \frac{1}{2}\}$ reflections obtained from different ZnCr_2O_4 polycrystalline samples. The best fit was obtained with the $\tau_1 + \tau_2$ model (see Fig. 10 (a)).

Sample	Rep.	T (K)	χ^2	R_{wp}
1	τ_1	1.5	4.915	.0664
	τ_1, τ_2		4.888	.0662
	τ_1, τ_2, τ_3		4.911	.0664
	τ_1, τ_6		4.998	.067
	τ_2, τ_3		4.995	.067
	2	τ_1, τ_2	7.3	1.368
3	τ_1, τ_2	2	4.003	.0592